

1 **The role of current sheet scattering in the proton**
2 **isotropic boundary formation during geomagnetic**
3 **storms**

4 **John D. Haiducek¹, Natalia Y. Ganushkina^{2,3}, Stepan Dubyagin³, Daniel T.**
5 **Welling^{2,4}**

6 ¹U.S. Naval Research Laboratory, Washington, DC, USA

7 ²Climate and Space Sciences, University of Michigan, Ann Arbor, MI, USA

8 ³Finnish Meteorological Institute, Helsinki, Finland

9 ⁴University of Texas at Arlington, Arlington, TX, USA

10 **Key Points:**

- 11 • We corrected estimates of the adiabaticity parameter K using in situ data, obtain-
- 12 ing consistent results between empirical and MHD models
- 13 • A significant fraction of the K estimates was below the threshold for current sheet
- 14 scattering
- 15 • Corrected K estimates are independent of $Symh-H^*$ and MLT, even for high val-
- 16 ues of K

This is the author manuscript accepted for publication and has undergone full peer review but has not been through the copyediting, typesetting, pagination and proofreading process, which may lead to differences between this version and the [Version of Record](#). Please cite this article as doi: [10.1029/2018JA026290](https://doi.org/10.1029/2018JA026290)

Corresponding author: John Haiducek, jhaiduce@umich.edu

Abstract

There is considerable evidence that current sheet scattering (CSS) plays an important role in isotropic boundary (IB) formation during quiet time. However, IB formation can also result from scattering by electromagnetic ion cyclotron (EMIC) waves, which are much more prevalent during storm time. The effectiveness of CSS can be estimated by the parameter $K = \frac{R_c}{r_g}$, the ratio of the field line radius of curvature to the particle gyroradius. Using magnetohydrodynamic (MHD) and empirical models, we estimated the parameter K associated with storm-time IB observations on the night side. We used magnetic field observations from spacecraft in the magnetotail to estimate and correct for errors in the K values computed by the models. We find that the MHD and empirical models produce fairly similar results without correction, and that correction increases this similarity. Accounting for uncertainty in both the latitude of the IB and the threshold value of K required for CSS, we found that 29–54% of the IB observations satisfied the criteria for CSS. We found no correlation between the corrected K and magnetic local time, which further supports the hypothesis that CSS played a significant role in forming the observed IBs.

1 Introduction

During geomagnetic storms, the shape and structure of the magnetotail can change rapidly and dramatically. This includes changes in the orientation of the current sheet, as well as rapid stretchings and dipolarizations. Although storms are driven by the solar wind, the ionosphere plays an important role in regulating the geomagnetic response to these solar wind inputs (e.g. Brambles et al., 2013, 2011; Daglis, 1997; Glocer, Tóth, Gombosi, & Welling, 2009; Welling & Liemohn, 2016). As such, characterizing the connections and interaction between the ionosphere and the magnetotail during storms is necessary in order to fully understand the behavior of the magnetosphere during storm conditions.

Most interaction between the magnetosphere and the ionosphere occurs through the flow of particles and currents along magnetic field lines. Characterizing the structure of these field lines can help us to determine the origins and destinations of plasma flows between the magnetosphere and ionosphere, and thus to better understand how the two regions interact with each other. Unfortunately, our ability to determine field line structure is limited by the very sparse distribution of satellite observations through-

49 out much of the magnetosphere. As a result, models of field line structure are often poorly
50 constrained, particularly during storm conditions when rapid changes in field line shape
51 pose an added challenge in determining the global system state at any given time.

52 To supplement the sparse magnetospheric observations, ionospheric observations
53 can be used to help better determine the state of the magnetotail. Ionospheric obser-
54 vations have the advantage of being at a low altitude where relatively large numbers of
55 satellites with fairly short orbital periods provide much better data coverage than is avail-
56 able in most of the magnetosphere. For instance, at present three National Oceanic and
57 Atmospheric Administration (NOAA) Polar Orbiting Environmental Satellites (POES)
58 satellites are in operation at altitudes of 800-900 km and with orbital periods around 100
59 minutes (<https://www.ospo.noaa.gov/Operations/POES/status.html>). Similarly, two
60 METOP satellites are in orbit at an 817 km altitude ([https://www.eumetsat.int/website/
61 home/Satellites/CurrentSatellites/Metop/index.html](https://www.eumetsat.int/website/home/Satellites/CurrentSatellites/Metop/index.html)), and several Defense Me-
62 teorological Satellite Program (DMSP) spacecraft orbit at a nominal 850 km orbit ([http://
63 www.au.af.mil/au/awc/space/factsheets/dmsp.htm](http://www.au.af.mil/au/awc/space/factsheets/dmsp.htm)).

64 In order to leverage ionospheric observations to help determine magnetotail struc-
65 ture, we must identify a feature in the ionosphere that maps to a known location in the
66 magnetosphere (or at least, to a location with known characteristics). This is the case
67 for the isotropic boundary (IB), which is a feature in the auroral zone of the ionosphere
68 characterized by a substantial change in the flux of downwelling particles. Poleward of
69 the IB, comparable fluxes are observed in directions parallel to and perpendicular to the
70 local magnetic field, while equatorward of the IB the flux in directions perpendicular to
71 the local magnetic field is much greater than the flux in the parallel direction. This ten-
72 dency has been observed by a number of satellites, including Injun 1 and 3, ESRO IA
73 and IB, NOAA, and DMSP (Imhof, Reagan, & Gaines, 1977; Newell, Sergeev, Bikkuz-
74 ina, & Wing, 1998; V. Sergeev, Sazhina, Tsyganenko, Lundblad, & Søråas, 1983; Søråas,
75 1972). The proton isotropic boundary is observed at all activity levels and in all mag-
76 netic local time (MLT) sectors (V. A. Sergeev, Malkov, & Mursula, 1993).

77 The change in loss-cone filling observed as a spacecraft transits the IB indicates
78 that the IB maps to a transitional region in the magnetosphere, which is characterized
79 by a substantial change in the rate of pitch angle scattering. Two mechanisms for this
80 have been proposed. Current sheet scattering (CSS) refers to a process in which parti-

cles undergo chaotic motion upon crossing the current sheet, resulting in changes to the particles' pitch angles (Büchner & Zelenyi, 1987; V. A. Sergeev et al., 1993; West, Buck, & Kivelson, 1978). This occurs when the radius of curvature, R_c , and the effective particle gyroradius, r_g , become comparable to each other, resulting in a violation of the first adiabatic invariant (Alfvén & Fälthammar, 1963; Büchner & Zelenyi, 1987; Delcourt, Sauvaud, Martin, & Moore, 1996; Tsyganenko, 1982). The second mechanism that has been proposed for IB formation is the scattering of particles by electromagnetic ion-cyclotron (EMIC) waves, in which plasma waves having oscillations near the particle gyrofrequency result in a violation of the first adiabatic invariant (Kennel & Petschek, 1966; Liang et al., 2014; V. A. Sergeev, Chernyaev, Angelopoulos, & Ganushkina, 2015; V. A. Sergeev, Chernyaeva, Apatenkov, Ganushkina, & Dubyagin, 2015).

Of the two mechanisms, the CSS process operates at all times and in all MLT sectors. A number of papers have identified CSS as the main (though not necessarily exclusive) mechanism for IB formation during quiet time (Ganushkina et al., 2005; Haiducek, Ganushkina, Dubyagin, & Welling, 2019 *accepted*; V. Sergeev & Tsyganenko, 1982; V. A. Sergeev et al., 1993). However, at times EMIC scattering may cause the IB to be observed at a lower latitude than would occur if CSS were the operative mechanism. This occurs primarily during storms and substorms (Dubyagin, Ganushkina, & Sergeev, 2018; Gvozdevsky, Sergeev, & Mursula, 1997; V. A. Sergeev et al., 2010; Søråas, Lundblad, Maltseva, Troitskaya, & Selivanov, 1980; Yahnin & Yahnina, 2007), though there is evidence that it occurs during quiet times as well (e.g. Popova, Yahnin, Demekhov, & Chernyaeva, 2018; V. A. Sergeev, Chernyaev, et al., 2015).

Distinguishing whether CSS or EMIC is the responsible mechanism for a particular IB observation is necessary for the application of IB observations to estimating magnetotail field geometry. When CSS is the responsible mechanism, the IB latitude can be used to estimate the amount of field line stretching in the magnetotail (Meurant et al., 2007; V. A. Sergeev & Gvozdevsky, 1995; V. A. Sergeev et al., 1993). This approach is likely to work well during quiet periods, but during storms it is expected that EMIC scattering will play a more significant role than it does in quiet time, because EMIC waves are more prevalent during storms. For instance, Erlandson and Ukhorskiy (2001) found that the EMIC wave occurrence rate increases by a factor of 5 during storm conditions over 10 years of observations, and Halford, Fraser, and Morley (2010) also found an increased EMIC occurrence rate during storm conditions. Determining whether EMIC or

114 CSS is responsible for IB formation at a given time and longitude requires estimating
115 the value $K = \frac{R_c}{r_g}$ associated with a given IB observation. K parameterizes the effec-
116 tiveness of the CSS process. V. Sergeev et al. (1983) proposed $K \leq 8$ as a threshold
117 condition for CSS scattering, while Delcourt, Malova, and Zelenyi (2006); Delcourt, Moore,
118 Giles, and Fok (2000); Delcourt et al. (1996) showed that CSS operates when $K \lesssim 1$ –
119 10, and V. A. Sergeev, Chernyaev, et al. (2015) suggested that CSS could be responsi-
120 ble for IB formation with K as high as 12. In the present work, recognizing that no sin-
121 gle value of K can be regarded as the definitive threshold, we adopt the range $K = 8$ –
122 13 as a nominal uncertainty range for the CSS scattering threshold, where the commonly
123 used $K \leq 8$ threshold serves as the lower end of the uncertainty range and the $K \leq$
124 13 value as the upper end of the uncertainty range, following the recent study by Dubya-
125 gin et al. (2018).

126 Computing K values associated with an IB observation requires tracing a magnetic
127 field line from the location of the observation to the point where it crosses the current
128 sheet. Both steps require a magnetic field model that can provide field vectors at arbi-
129 trary points within the magnetosphere. Most previous studies to do this have employed
130 empirical models such as the Tsyganenko models (e.g. Dubyagin et al., 2018; Ganushk-
131 ina et al., 2005; V. A. Sergeev, Chernyaev, et al., 2015; V. A. Sergeev et al., 1993), but
132 two have done so using magnetohydrodynamic (MHD) models (e.g Haiducek et al., 2019
133 *accepted*; Ilie, Ganushkina, Toth, Dubyagin, & Liemohn, 2015). Ilie et al. (2015) obtained
134 K values for IB observations during a quiet period, and obtained unrealistically high K
135 values for conditions in which CSS was expected to be the dominant mechanism. Haiducek
136 et al. (2019 *accepted*) simulated the same quiet period using different model settings. Haiducek
137 et al. (2019 *accepted*) obtained lower K values than those of Ilie et al. (2015), and demon-
138 strated that these values could be corrected using in situ magnetic field observations, con-
139 cluding that the quiet time IB observations were likely the result of CSS and not EMIC.

140 The work of Haiducek et al. (2019 *accepted*) demonstrated the use of MHD to es-
141 timate K during quiet conditions, and obtained results that were consistent with those
142 derived from empirical models for the same time period. However, the circumstances in
143 which MHD is likely to be most advantageous for studying the IB are during storm con-
144 ditions. Through simulations of storms, the physics incorporated into an MHD model
145 can be used to shed light on the causes of storm-time dynamics. Several previous pa-
146 pers have presented K estimates during storm conditions, but all have used empirical

147 models which were constructed from fits to historical satellite observations (e.g. Dubya-
148 gin et al., 2018; Ganushkina et al., 2005; V. A. Sergeev et al., 1993). Since MHD mod-
149 els simulate the physics of the magnetosphere rather than presenting a fit to historical
150 observations, it has the potential to reproduce features and dynamics of storm events
151 that may be missed by empirical models, as well as provide additional information that
152 can shed light on the causes of any dynamics that are reproduced by the model. The use
153 of MHD to explore IB properties during disturbed conditions (specifically, during a sub-
154 storm) was previously demonstrated by Gilson, Raeder, Donovan, Ge, and Kepko (2012),
155 but no comparison of K estimates with IB observations was performed. To date, no pub-
156 lished work has used MHD to explore IB properties during a geomagnetic storm.

157 The goal of the present work is to estimate what fraction of IB observations might
158 be the result of CSS during storm conditions, and to test whether MHD and empirical
159 models produce consistent values of K during storm conditions. We estimate K using
160 multiple MHD simulations and multiple empirical models, in order to obtain a better
161 representation of the range of variability for K than would be possible using any single
162 model alone. Next we compare our K values with the $K = 8$ and $K = 13$ threshold
163 conditions to estimate what fraction of the IB observations may have been the result of
164 CSS (as opposed to EMIC wave scattering). We estimate errors in the model output by
165 comparing with in situ magnetic field observations, and apply procedures from Dubya-
166 gin et al. (2018) and Haiducek et al. (2019 *accepted*) to correct for these errors. The present
167 work is the first to use MHD to explore IB properties during a geomagnetic storm, and
168 the first to estimate K using MHD during disturbed conditions.

169 The paper is organized as follows. Section 2 provides a description of the time pe-
170 riod chosen and the observational data used. Section 3 describes the procedures used to
171 estimate K , and the details of the MHD simulations. Section 4 presents a validation of
172 the MHD magnetic fields against in situ observations. Sections 5 and 6 present results
173 from the MHD and empirical models, respectively. Section 7 outlines the procedure for
174 correcting the K values and presents the overall results for K and the corrections, and
175 the paper concludes with section 8.

193 **Figure 1.** Solar wind driving parameters used in the study, along with geomagnetic indices
 194 parameterizing the magnetospheric response. (a) u_x component of bulk velocity, in GSM coor-
 195 dinates, (b) proton density ρ , (c) temperature, (d) IMF B_z , (e) *Symh-H*, (f) *Kp*, (g) *AL*. The
 196 beginning of the storm is marked with a vertical line.

176 2 Event and observations

177 We chose the time period of 2100 UT on 4 April, 2010 to 1400 UT on 6 April, 2010
 178 for our analysis. The major feature of this time period is a moderate storm with a min-
 179 imum *Symh-H* of -90 nT and a maximum *Kp* of 7.7. This storm was the result of a coro-
 180 nal mass ejection observed at 0954 UT 3 April. The northern flank of the CME reached
 181 the Sun-Earth L1 Lagrange point around 0755 UT on 4 April, and was followed by the
 182 passage of a magnetic cloud from around 1200 UT on 5 April until 1320 UT on 6 April
 183 (Liu, Luhmann, Bale, & Lin, 2011; Möstl et al., 2010). Solar wind parameters from this
 184 time period are shown in Figures 1a–1d. The beginning of the storm is marked with a
 185 vertical line. Observational data shown in Figure 1 come from the 1-minute OMNI data
 186 set provided by the National Aeronautics and Space Administration (NASA) Goddard
 187 Spaceflight Center (GSFC). The beginning of the storm is marked by a sudden increase
 188 in solar wind speed between 0800 and 0900 UT on 5 April (see the u_x velocity compo-
 189 nent in Figure 1a), accompanied by sharp increases in solar wind density ρ (Figure 1b)
 190 and temperature (Figure 1c). The B_z component of the interplanetary magnetic field
 191 (IMF, Figure 1d) abruptly became more negative at the same time, and oscillated rapidly
 192 for the next few hours.

197 To quantify the magnetospheric response to the storm, we use the *Symh-H*, *Kp*,
 198 and *AL* indices. The latitude of the IB has been found to be sensitive to all three of *Symh-*
 199 *H* (e.g. Asikainen, Maliniemi, & Mursula, 2010; Dubyagin et al., 2013, 2018; Ganushk-
 200 ina et al., 2005; Hauge & Søråas, 1975; Lvova, Sergeev, & Bagautdinova, 2005; Søråas,
 201 1972; Søråas, Aarsnes, Oksavik, & Evans, 2002), *Kp* (e.g. V. A. Sergeev et al., 1993; Søråas,
 202 1972; Yue et al., 2014), and *AL* (e.g. Dubyagin et al., 2013; Lvova et al., 2005; Søråas,
 203 1972).

204 The *Symh-H*, *Kp*, and *AL* indices during 4–6 April 2010 are shown in Figures 1e,
 205 1f, and 1g. From the *Symh-H* index (Figure 1e), a storm sudden commencement can

206 be seen just after 0800 UT on 5 April, followed by a sharp decrease in *Symh-H*. The
207 minimum *Symh-H* of -90 nT does not occur until almost 24 hours later. The maximum
208 *Kp* of 7.7 occurred around 0900 UT on 5 April (Figure 1f), and *Kp* remained at or above
209 3 throughout the event. The *AL* index (Figure 1g) dropped rapidly after the storm com-
210 mencement, reaching a minimum of -2,152 nT but quickly recovering.

211 Observations of isotropic boundaries were obtained using the Medium Energy Pro-
212 ton and Electron Detector (MEPED) instruments (Evans & Greer, 2000) onboard five
213 NOAA/POES and one METOP spacecraft. This instrument consists of two telescopes
214 which detect proton fluxes in four energy bands between 30 and 6900 keV. The telescopes
215 are referred to as the 0° and 90° telescope, after their approximate directions relative to
216 the spacecraft's zenith. The 0° telescope points away from the Earth, while the 90° telescope
217 is roughly perpendicular to the 0° telescope and points along the spacecraft's velocity vec-
218 tor. When the spacecraft is at relatively high latitudes, this configuration results in the
219 0° telescope mainly detecting precipitating particles, while the 90° telescope mainly de-
220 tects locally trapped particles.

221 IB locations were identified from the MEPED P1 energy channel. The nominal en-
222 ergy range of this channel is 30–80 keV, but in reality the lower energy limit is somewhat
223 higher than 30 keV and varies among the satellites due to degradation of the detectors
224 over time. We used the low energy limits given by Asikainen, Mursula, and Maliniemi
225 (2012), and these are reproduced in Table S1 in the supporting information. In addition
226 to variance between the spacecraft, the 90° telescope degrades more rapidly than the 0°.
227 We recalibrate the 90° flux to correspond to the 0° cutoff energy using the procedure given
228 in the Appendix of Dubyagin et al. (2018). Using these corrected fluxes, we found IB cross-
229 ings with the procedure described in Dubyagin et al. (2018). It should be noted that there
230 can be significant uncertainty associated with the determination of IB locations from MEPED
231 data during storm periods. To address this, the Dubyagin et al. (2018) procedure defines
232 a high latitude (HL) and low latitude (LL) limit of the IB based on the MEPED data,
233 which we use to estimate the uncertainty range for the IB latitude.

234 Rather than using all available IB observations, we limit our analysis to those for
235 which in situ magnetic field observations were available in the magnetotail from one or
236 more spacecraft that were conjugate with the location of the IB observation in the iono-
237 sphere. To consider a spacecraft as conjugate with the IB observation, we require it be

267 **Figure 2.** (a) Locations of THEMIS A and GOES 11 at the times of all the IB observations.
 268 (b) and (c) Relative positions of THEMIS A, D, and E at 0700 UT on 5 April.

238 within one hour MLT of the location of the IB observation. In addition, we require the
 239 conjugate spacecraft to be located near the equatorial plane between 4 and 12 R_E from
 240 the Earth. Only IB observations from the night side were used. The spacecraft meet-
 241 ing these criteria were Time History of Events and Macroscale Interactions during Sub-
 242 storms (THEMIS, Auster et al., 2008; McFadden, Carlson, Larson, Bonnell, et al., 2008;
 243 McFadden, Carlson, Larson, Ludlam, et al., 2008) A, D, and E, and Geostationary Op-
 244 erational Environmental Satellite (GOES Singer, Matheson, Grubb, Newman, & Bouwer,
 245 1996) 11–15. Representative locations for these spacecraft are shown in Figure 2. In to-
 246 tal, 127 HL IB observations and 127 LL IB observations were found on the night side
 247 for which at least one of the GOES or THEMIS satellites was conjugate with the IB ob-
 248 servation. Exact times and locations of each IB observation are provided in the support-
 249 ing information.

250 Figure 2a shows examples of conjugate satellite positions in the x - y geocentric so-
 251 lar magnetospheric (GSM) plane, with THEMIS A locations marked with turquoise pen-
 252 tagons and GOES 11 locations with purple triangles. THEMIS D and E, not shown, had
 253 orbits somewhat similar to that of THEMIS A, while GOES 12–15 were in geosynchronous
 254 orbits similar to that of GOES 11. Satellite locations were obtained using orbital data
 255 from the Satellite Situation Center Web (<https://sscweb.gsfc.nasa.gov>). The mark-
 256 ers in Figure 2a show satellite positions for all the times at which the respective satel-
 257 lite was conjugate with an IB observation.

258 Figures 2b and 2c show the relative positions of THEMIS A, D, and E at 0700 UT
 259 on 5 April, when all three were near apogee. Figure 2b shows the x - y (GSM) plane, while
 260 Figure 2c shows the y - z plane. THEMIS E is depicted as a purple hexagon, and THEMIS
 261 D as an orange diamond. Note that the spacecraft are spaced relatively closely in x and
 262 y , but THEMIS A is separated significantly in the z direction from THEMIS D and E.
 263 This configuration allows the estimation of gradients in the z direction by computing a
 264 difference between THEMIS A and E. Configurations like this existed a significant part
 265 of the time interval under study, and we used such satellite configurations to estimate
 266 R_c and its influence on K .

3 Methodology

For each of the 227 IB crossings identified as described in the previous section, we trace a magnetic field line from the location of the IB observation, and compute $K = \frac{R_c}{r_g}$ at the point along the field line that is farthest from the Earth. Both the field line tracing and the computation of K require a model to estimate the magnetic fields. For this purpose we use MHD simulations executed using the Space Weather Modeling Framework (SWMF) (Tóth et al., 2005) and the T01 (Tsyganenko, 2002), TS05 (Tsyganenko & Sitnov, 2005), and TA16 (Tsyganenko & Andreeva, 2016) empirical magnetic field models. The set-up for the SWMF simulations is described in detail later in this section, and the empirical models are described in section 6.

The point of maximum distance from the Earth was chosen as an estimate of where the field line crosses the current sheet. Although intuitively the point of minimum $|\mathbf{B}|$ would indicate the current sheet, we found that in some cases the field line is “pinched” around the current sheet, producing an additional pair of local minima in $|\mathbf{B}|$ which are sometimes lower than the minimum that occurs when the field line crosses the current sheet. As a result the maximum distance proved to be a more robust indicator of where the field line crossed the current sheet. In a few cases the field line traced from the IB location was found to be open (extending outside the MHD domain), and such cases were excluded from further analysis.

At the point of maximum distance from the Earth along the field line, we compute R_c , the field line radius of curvature, given by

$$R_c = \frac{1}{|(\mathbf{b} \cdot \nabla)\mathbf{b}|}, \quad (1)$$

where \mathbf{b} is the unit vector in the direction of the local magnetic field. The gradient $\nabla\mathbf{b}$ is computed using a two-point centered difference scheme on the MHD grid. The effective gyroradius r_g is computed for protons whose energy is equal to the low energy limit of the respective detector, as given in Table S1 in the supporting information. We then use these estimates of R_c and r_g to compute K . We rejected any K estimates below 0.01.

Our SWMF simulations use the Block Adaptive Tree Solar-Wind, Roe-type Upwind Scheme (BATS-R-US) MHD code (DeZeeuw, Gombosi, Groth, Powell, & Stout,

298 2000; Powell, Roe, Linde, Gombosi, & De Zeeuw, 1999). This is coupled with the Rice
 299 Convection Model (RCM) (Sazykin, 2000; Toffoletto, Sazykin, Spiro, & Wolf, 2003; Wolf
 300 et al., 1982) and the Ridley Ionosphere Model (RIM) (Ridley, Gombosi, & De Zeeuw,
 301 2004; Ridley & Liemohn, 2002). The inputs to the model are solar wind parameters (ve-
 302 locity, density, temperature, and magnetic field) and F10.7 solar radio flux, as shown in
 303 Figure 1. Solar wind parameters were obtained from the 1-minute OMNI data set. F10.7
 304 flux was obtained from the noontime flux observed at Penticton, British Columbia and
 305 published online at [ftp://ftp.geolab.nrcan.gc.ca/data/solar_flux/daily_flux_values/](ftp://ftp.geolab.nrcan.gc.ca/data/solar_flux/daily_flux_values/fluxtable.txt)
 306 `fluxtable.txt` (Tapping, 2013).

307 We ran three SWMF simulations, with the same inputs but with different grid res-
 308 olutions and differences in numerical schemes and coupling parameters. By comparing
 309 the results obtained with the three simulations we are able to assess qualitatively how
 310 sensitive the model-derived K values are to the model settings. The three simulations
 311 are the same as those in Haiducek et al. (2019 *accepted*), and details on the settings can
 312 be found there and in Haiducek, Welling, Ganushkina, Morley, and Ozturk (2017) which
 313 shares some of the settings in common. We describe them briefly here:

- 314 • **SWMFa**: Same settings as Ilie et al. (2015), but with modifications to improve
 315 stability (details in Haiducek et al. (2019 *accepted*)). 4 million cell grid, with 0.25
 316 R_E cell size in the expected region of IB formation.
- 317 • **SWMFb**: A 2 million cell grid, with a finer resolution the mid tail (48–120 R_E)
 318 compared with SWMFa, but courser resolution farther down-tail (beyond 120 R_E).
 319 0.25 R_E cell size in the expected region of IB formation. Settings described in de-
 320 tail in Haiducek et al. (2017) where this model configuration is referred to as the
 321 “Hi-res” configuration.
- 322 • **SWMFc**: A 1 million cell grid with settings based on those used operationally
 323 by the NOAA Space Weather Prediction Center. 0.5 R_E cell size in the expected
 324 region of IB formation. Settings are described in detail in Haiducek et al. (2017),
 325 where this model configuration is referred to as the “SWPC” configuration.

326 During execution of the simulations, magnetic field lines were traced from the lo-
 327 cations of each IB observation once every minute of simulation time. Within the MHD
 328 domain, the field lines were traced using a third order Runge-Kutta scheme with a sec-
 329 ond order error estimation and adaptive step size. Since the inner boundary of the MHD

330 domain was set to $2.5 R_E$, well above the altitude of the IB observations, the IB loca-
331 tions were mapped to $2.5 R_E$ prior to tracing through the MHD domain. This was done
332 by transforming the IB locations into altitude adjusted corrected geomagnetic coordi-
333 nates (AACGM, Baker & Wing, 1989) with the reference height set to 0 km, and then
334 mapping to $2.5 R_E$ using a dipole field. The use of AACGM coordinates minimizes the
335 influence of non dipole harmonics on the mapping.

336 4 Comparison of MHD magnetic fields with in situ observations

337 Before analyzing the IB observations using MHD, we made a comparison of the MHD
338 magnetic fields with in situ observations. This provides a means to verify that the sim-
339 ulation accurately reproduces the magnetic field in the magnetotail. An example of this
340 comparison is shown in Figure 3, which contains plots of simulated and observed mag-
341 netic fields along the orbit of the THEMIS A satellite. (Similar plots for THEMIS D and
342 E and GOES 11–15 are included in the supporting information.) Figures 3a, 3c, and 3e
343 show the x , y , and z (GSM) components of the total magnetic field, while Figures 3b,
344 3d, and 3f show the same for the external field. In all of these plots, the observed field
345 is depicted as a light blue curve, and the SWMFa, SWMFb, and SWMFc simulations
346 are shown as thinner curves colored in medium blue, orange, and green, respectively. THEMIS
347 data were downloaded and calibrated using the THEMIS Data Analysis Software (TDAS,
348 <http://themis.ssl.berkeley.edu/software.shtml>). Magnetic field data are shown
349 only for times when the satellite was at least $4 R_E$ away from the Earth, since closer lo-
350 cations do not satisfy our selection criteria for analysis. The time period shown is 0009
351 UT on 4 April to 1400 UT on 6 April 2010, an interval which includes the times of all
352 the IB observations used in this study.

353 The external magnetic field shown in Figures 3b, 3d, and 3f was obtained by re-
354 moving dipole component of the Earth’s intrinsic field, evaluated using Geopack ([http://](http://geo.phys.spbu.ru/~tsyganenko/modeling.html)
355 geo.phys.spbu.ru/~tsyganenko/modeling.html). We remove only the dipole compo-
356 nent because that is how the intrinsic field is represented within SWMF. As mentioned
357 in the previous section, the influence of non-dipole harmonics on the K estimations is
358 minimized by converting the IB locations to AACGM coordinates prior to tracing the
359 fields in SWMF. Points where the spacecraft is closer than $4 R_E$ to the Earth have been
360 excluded from the plot, since such points do not meet the criteria for selection of con-
361 jugate points with IB observations.

362 Multiple sign changes in B_x can be seen in Figure 3a, which are indicative of cur-
363 rent sheet crossings. This occurs most noticeably between 0900 and 1600 UT on 5 April
364 during the initial phases of the storm, and a few additional current sheet crossings oc-
365 cur between 2100 and 0200 UT on 5–6 April and around 1200 on 6 April.

366 From Figure 3, it can be seen that the SWMF simulations reproduce many of the
367 major variations in the observed field. During the quiet period before the storm, the er-
368 ror generally remains within 25 nT in all three components (Figures 3b, 3d, and 3f).

369 **Figure 3.** Magnetic field components of the total field in GSM coordinates at the THEMIS A
370 satellite, observed and simulated, from 0009 UT on 5 April to 1400 UT on 6 April, 2010.

371 At the storm sudden commencement around 0900 UT on 5 April, a sharp increase
372 in observed B_z occurs, and is accompanied by an increase in B_x and oscillations in B_y .
373 Similar behavior occurs in the simulations, but the timing is slightly different and the
374 variation in B_x and B_y is weaker than observed. After the storm sudden commencement,
375 all three simulations reproduce the general trend in the observations, in which B_x and
376 B_y become more negative, and B_z increases sharply and then decreases. Like the obser-
377 vations, rapid fluctuations in B_x and B_y are apparent, though the magnitude of these
378 fluctuations is weaker and the timing is not exactly the same as the observations. In some
379 cases this results in particularly large magnetic field errors such as the spike in B_x around
380 1200 UT on 5 April which was not reproduced by any of the simulations. The somewhat
381 weaker magnitude of oscillations in the model output may indicate a thicker or weaker
382 current sheet compared with reality. From about 1300 to 1800 UT on 5 April the sim-
383 ulations produce more negative B_x than observed, which suggests that the model cur-
384 rent sheet is more northerly than actual during that time, or that the current in the model
385 is stronger than actual. During the next orbit of the spacecraft (2100 UT on 5 April to
386 1400 UT on 6 April) the conditions are somewhat quieter, with the largest disturbance
387 being a brief but substantial (≈ 60 nT) oscillation in B_x and B_y around 2400 UT and
388 a weaker one around 0300 UT, neither of which is reproduced by the simulations. Some
389 fairly large (≈ 50 nT) errors occur in SWMFb between 2200 and 2400. Aside from the
390 aforementioned periods, the simulation fields during the second orbit remained gener-
391 ally within 20 nT of the observations.

5 MHD results

Figure 4 shows the behavior of the Kp and $Symh-H$ indices and the IB mapping parameters over the course of the storm. Figures 4a and 4b show Kp and $Symh-H^*$, respectively, with the observations drawn with thick light-blue lines and the SWMF simulations with thinner lines (SWMFa in blue, SWMFb in orange, and SWMFc in green). $Symh-H^*$ is computed from the $Symh-H$ index by applying a correction for solar wind dynamic pressure p_{dyn} using the same formula as the Dst^* index given in Burton, McPherson, and Russell (1975). This correction removes the contribution of the magnetopause current to $Symh-H$. Figure 4c shows the absolute value of the AACGM magnetic latitude at which each IB was observed. Observations from the equatorward boundary of the IB (abbreviated as LL for low latitude) are shown in blue, while observations from the poleward boundary of the IB (abbreviated as HL for high latitude) are shown in red. The two boundaries are identified according to the procedure from Dubyagin et al. (2018), as discussed in the previous section. Figure 4d shows the MLT of each IB observation, with red and blue markers identifying the HL and LL IB observations as in Figure 4c. Figure 4e shows the maximum distance from the Earth along the field line traced from each of these IB observations, which as discussed earlier is used to estimate the current sheet crossing location. The points in Figure 4e include both the HL and the LL sets. The results for each SWMF simulation are shown, with SWMFa depicted as blue circles, SWMFb as orange squares, and SWMFc as green triangles. Figure 4f shows the values of K obtained from the MHD solution at the locations depicted in Figure 4e.

Figure 4. IB parameters and geomagnetic indices as a function of time. (a) Kp index, observed and simulated, (b) $Symh-H^*$ index, observed and simulated, (c) Absolute value of magnetic latitude of the IB observations, (d) MLT of the IB observations, (e) Maximum down-tail distance of the field lines mapped from the IB locations, for each of the three MHD simulations, (f) K computed from the MHD solution at the farthest point of each field line.

From Figure 4a it is apparent that the simulated Kp is generally within 1 Kp unit of the observations, except for a Kp of zero computed at the beginning of the simulations, an early increase in Kp three hours before the storm begins and a decrease in Kp reported by SWMFc near the end of the storm. Figure 4b shows that the simulated $Symh-$

422 H^* values are generally within 20 nT of the observed *Symh-H**, with exceptions being
423 an overestimation (in magnitude) of *Symh-H** during some of the stronger periods of
424 the storm, and an underestimation (in magnitude) of *Symh-H** by SWMFc near the end
425 of the storm.

426 From Figure 4c it is apparent that the IB latitude varies over time during the storm.
427 The few quiet time IB observations are spaced fairly close together in latitude, and their
428 latitude gradually increases from around 63 to 66 degrees between 0300 and 0800 UT.
429 When the storm commences around 0900 UT, the IB latitude sharply decreases to around
430 62 degrees. 62 degrees remains the most common latitude for the next several hours, but
431 outlier IB observations occur as high as 73 degrees. After 2000 UT, the number and sever-
432 ity of high-latitude outliers decreases somewhat, and the lower latitude limit of IB ob-
433 servations initially decreases to 60 degrees around 2400 UT on 5 April, then increases
434 gradually until reaching 64 degrees around 1200 UT on 6 April.

435 Figure 4d shows that there are distinct trends in MLT over time as well. These trends
436 are due mainly to the orbital motion of the conjugate satellites over time. Since IB lat-
437 itude is known to vary with MLT (e.g. Asikainen et al., 2010; DUBYAGIN et al., 2018; Ganushk-
438 ina et al., 2005; Lvova et al., 2005), these variations in MLT are probably responsible
439 for some of the variations in IB latitude seen in Figure 4c.

440 The distances in Figure 4e reflect the latitudes shown in Figure 4c: The distances
441 tend to increase when the IB latitudes increases, and decrease when the IB latitudes de-
442 crease. This correspondence between latitude and mapping distance is expected. For a
443 dipole field, distance increases monotonically with increasing latitude of field line foot-
444 points, and the stretched geometry of the night side magnetosphere results in an even
445 faster increase. A similar correspondence with latitude can be seen in Figure 4f, but the
446 behavior is reversed, with the K estimates tending to decrease with increasing IB lat-
447 itude.

448 The overall range of K estimations from the SWMF simulations is shown in the
449 first two rows of Table 1, which shows the total number of usable K estimations in each
450 row, 25th percentile, median, and 75th percentile of the K estimations. Results from all
451 three SWMF simulations are combined together in Table 1, and only usable K estimates
452 are included (those for which the traced field line was closed, and K was greater than
453 0.01). The percentiles for $K = 8$ and $K = 13$ (i.e., the percentage of K values falling

below $K = 8$ and $K = 13$) are also shown. The number of K estimates falling below these thresholds provides an estimate for what percentage of the IB's might have been formed by CSS. By using two different thresholds we are able to provide a rough estimate of the uncertainty range for this percentage. The $K_{\text{crit}} = 8$ threshold, as discussed in the Introduction, was originally introduced by V. Sergeev et al. (1983) as a rough estimate of the threshold condition for CSS, and has been widely adopted by other researchers. In the present work, we adopt $K = 8$ as a probable low end of the uncertainty range for K_{crit} . For the upper end, we note that V. A. Sergeev, Chernyaev, et al. (2015) found differences in the properties of IB's above and below $K = 13$, while Dubyagin et al. (2018) found that $4.5 < K < 13$ fell within $1 R_E$ of where $K = 8$ for 90% of field configurations produced by the TS05 model, and Haiducek et al. (2019 *accepted*) obtained corrected K values falling mostly below $K = 11$ for carefully chosen IB observations in quiet conditions. Based on these results, we have adopted $K = 13$ as an approximate upper end of the uncertainty range for K_{crit} . The results in Table 1 are separated according to whether they were obtained from observations of the high-latitude (HL) or low-latitude (LL) boundary of the IB. Both the medians and the interquartile ranges of K are somewhat higher for the LL set, consistent with the tendency noted in the previous paragraph that increases in IB latitude are associated with decreases in K and vice versa. The remaining rows of Table 1 will be discussed later in the paper.

The negative correlation between the estimated K in the IB formation region and IB latitude can be explained by both the EMIC wave and the CSS mechanisms, noting that the value of K can be approximated as

$$K = \frac{R_c}{r_g} \approx \frac{qB_z^2}{\sqrt{2mE}dB_r/dz}, \quad (2)$$

where q denotes the particle charge, m the particle mass, and E the particle energy. B_r is the radial component of magnetic field in GSM coordinates, given by

$$B_r = \frac{x B_x + y B_y}{\sqrt{x^2 + y^2}}. \quad (3)$$

B_z near the equatorial plane decreases as $\frac{1}{r^3}$ in a dipole field, and the stretched field lines in the night side magnetosphere result in even faster decrease. This tends to result in an inverse relationship where K decreases with increasing distance. If the IB forma-

Model type	IB set	n	25th percentile	Median	75th percentile	$K \leq 8$ percent-age	$K \leq 13$ percent-age	y axis intercept	Intercept 95% CI
<i>Uncorrected K</i>									
SWMF	HL	254	8.18	16.7	30.9	23.6	38.6	—	—
SWMF	LL	339	9.69	18.9	33.1	20.1	35.1	—	—
Empirical	HL	254	3.93	10.3	15.9	40.2	61.4	—	—
Empirical	LL	273	6.01	12.3	20.0	31.5	52.7	—	—
Both	HL	508	6.32	13.0	22.4	31.9	50.0	—	—
Both	LL	612	7.98	15.4	27.9	25.2	43.0	—	—
<i>K^* correction</i>									
SWMF	HL	254	7.21	12.8	20.3	29.1	51.6	11.5	[10.3, 12.8]
SWMF	LL	339	8.26	14.9	24.6	23.3	42.2	13.6	[12.4, 14.9]
Empirical	HL	254	4.99	9.61	15.7	42.5	66.1	7.87	[7.01, 8.83]
Empirical	LL	273	6.95	12.7	19.3	31.1	51.3	10.7	[9.54, 11.9]
Both	HL	508	5.61	10.8	17.1	36.4	59.4	9.35	[8.62, 10.1]
Both	LL	612	7.54	13.8	21.5	27.3	46.2	12.1	[11.3, 13.0]

473

Table 1. Values summarizing the distribution of K and K^* .

482 tion process is independent of K (as is the case for EMIC wave scattering), the IB lat-
 483 itude roughly corresponds to the distance of the IB field line in the equatorial plane, re-
 484 sulting in a negative correlation between IB latitude and K . For CSS-driven IB forma-
 485 tion, this relationship between K and distance from the Earth should be absent since
 486 we are computing K at points mapped from the IB, and IB formation through CSS is
 487 directly controlled by K . However, if the simulation fails to respond to fast variations
 488 in the magnetosphere, the IB will be projected to (and K estimated at) points distributed
 489 around the true IB formation region, and the deviation of the model K estimates from
 490 reality will reflect the average radial profile of K , with associated negative correlation
 491 between K and IB latitude. Thus, the approximately inverse relationship between K and
 492 distance seen in Figures 4e and 4f could indicate a failure of the model to reproduce the
 493 true magnetic field geometry, or it could indicate that some of the observed IB's were
 494 formed by EMIC scattering.

495 Noting the quadratic dependence of K on B_z in equation (2), we estimate the er-
 496 ror in B_z at the locations where K was estimated by computing the B_z errors at the space-
 497 craft that are conjugate with each IB location. The conjugate spacecraft include at least
 498 one and in some cases several of the GOES and THEMIS satellites. We denote the av-
 499 eraged error as $\overline{\Delta B_z}$. Figure 5 shows K as a function of $\overline{\Delta B_z}$ for the points from Fig-
 500 ure 4. Figure 5a shows the HL points, while 5b shows the LL points. Results from each
 501 model run are depicted using the same color and marker scheme as Figure 4. Fit lines
 502 are drawn in black on top of the points. Note that a logarithmic scale is used for the y
 503 axis and a linear fit has been performed on the transformed data; the reason for this will
 504 be explained later. Points that mapped to within $8 R_E$ of the MHD domain boundaries
 505 have been excluded.

506 **Figure 5.** K as a function of $\overline{\Delta B_z}$ for all three MHD simulations, computed for locations
 507 mapped from IB observations in the HL data set (a) and the LL data set (b). Black lines show
 508 linear fits (in log space) to the data.

509 Figure 5 shows that K increases with increasing $\overline{\Delta B_z}$. Noting the quadratic de-
 510 pendence of K on B_z in equation (2), K at the IB location will be overestimated if the
 511 model overestimates B_z . In addition, this effect is strengthened by the mapping error;

512 because understretched model fields map the IB field line closer to the Earth, in the re-
513 gion of higher K .

514 From Figure 5 it appears that the SWMF has a tendency to over-predict B_z , with
515 a substantial fraction of the ΔB_z values falling between 0 and 20 nT. Indeed, we found
516 that the SWMF simulations overestimated $\overline{\Delta B_z}$ about 65–70% of the time (more detailed
517 statistics for $\overline{\Delta B_z}$ are given in Table S2 in the supporting information). Most of the K
518 values corresponding to $\overline{\Delta B_z} > 0$ fall within the interquartile ranges shown in the first
519 two rows of Table 1. Anomalously low K values ($K \lesssim 4$) appear only when $\overline{\Delta B_z} \lesssim$
520 12. Despite the correlation between K and ΔB_z , K values seem to be constrained to $K \lesssim$
521 100, with K remaining below that threshold even for the largest overestimations of B_z .

522 6 Empirical results

523 In this work we use the empirical magnetic field models T01, TS05, and TA16. All
524 three are available at <http://geo.phys.spbu.ru/~tsyganenko/modeling.html>. These
525 models operate by computing a sum of analytical functions of a set of solar wind and
526 geomagnetic activity parameters. In the case of T01 and TS05 these functions represent
527 specific current systems, while in TA16 they are radial basis functions with no correspon-
528 dence among the known current systems in the magnetosphere.

529 We now describe some of the features of these models that are relevant to estimat-
530 ing K . In the T01 model, the current sheet thickness is constant, but the inner edge of
531 the tail current moves Earthward with increasing activity, and the tail current radial pro-
532 file is controlled by two independent sub-modules.

533 The TS05 model was designed specifically to model storm-time conditions, and it
534 was constructed by fitting to data from storm periods. The position and thickness of the
535 TS05 tail current vary with activity, and are parameterized by a complex integral func-
536 tions of the time history of solar wind parameters.

537 While the T01 and TS05 models used pre-determined functions to define the mag-
538 netospheric current systems, the TA16 model replaces these ad hoc functions with a sum
539 of radial basis functions controlled by driving parameters (Newell, Sotirelis, Liou, Meng,
540 & Rich, 2007). This avoids imposing assumptions about the form of the current systems
541 through the choice of fitting functions. However, the limited number of observations avail-
542 able for fitting precludes resolving fine spatial structures by this method.

543 We traced field lines from the IB locations (in AACGM coordinates) using each of
 544 these models, and with a dipole representation for intrinsic field of the Earth. Geopack
 545 was used to perform the actual tracing of the field lines. As with the SWMF simulations,
 546 $K = \frac{R_c}{r_g}$ was estimated at the point of maximum distance from the Earth along each
 547 field line, using the detector cutoff energies (Table S1 in the supporting information) to
 548 estimate r_g and equation (1) to estimate R_c . The output from the models was also com-
 549 puted at the locations of the THEMIS spacecraft for comparison with observations.

550 Figure 6 shows the K values obtained from the empirical models as a function of
 551 $\overline{\Delta B_z}$, which as with the SWMF simulations represents the model error in B_z , averaged
 552 over the THEMIS spacecraft that were conjugate with each IB observation. Points from
 553 T01 are shown as red diamonds, TS05 as purple right-pointing triangles, and TA16 as
 554 brown left-pointing triangles. Figure 6a shows the HL data, and Figure 6b shows the LL
 555 data. A least-squares fit (in log-space) through all the points is shown in black. It ap-
 556 pears that the three models performed similarly, and a general similarity with the SWMF
 557 simulations is also apparent, although the K values are somewhat lower and the tendency
 558 to overestimate B_z is less pronounced.

559 **Figure 6.** K as a function of $\overline{\Delta B_z}$ for the empirical models, computed for locations mapped
 560 from IB observations in the HL data set (a) and LL data set (b). The black lines show a linear fit
 561 (in log space) to the data.

562 From Figure 6 it is also apparent that the T01 model has a tendency toward un-
 563 derestimation of $\overline{\Delta B_z}$, while the TS05 and TA16 models tend toward overestimation of
 564 $\overline{\Delta B_z}$. This is further supported by the metrics for $\overline{\Delta B_z}$ given in Table S2 of the support-
 565 ing information.

566 The third and fourth rows of Table 1 summarize the range of K obtained from the
 567 empirical models. As with the SWMF results, the empirical model results in the table
 568 were obtained by combining the results from all the empirical models together. K es-
 569 timates below 0.01 were excluded from the results. Like the SWMF estimates of K , the
 570 median, 25th, and 75th percentiles are all higher for the LL data set than for the HL data
 571 set. K values at all three quartiles are lower than they are for SWMF, indicating a sys-

572 tematic tendency toward lower K values with the empirical models. On the other hand,
573 the interquartile ranges overlap substantially between the two classes of models.

574 **7 K correction**

575 We have seen that both the SWMF simulations and the empirical models have ten-
576 dencies to over- or under-estimate B_z relative to in situ observations in the magnetotail.
577 However, both the SWMF simulations and the empirical models exhibit a positive cor-
578 relation between K and $\overline{\Delta B_z}$, which is consistent with the quadratic relationship between
579 K and B_z seen in equation (2). This relationship enables us to correct the model-derived
580 K values for the known errors in B_z , using the correction procedure previously described
581 in Dubyagin et al. (2018) and Haiducek et al. (2019 *accepted*). The procedure consists
582 of taking the logarithm of both sides of equation (2), then linearizing to obtain a linear
583 equation of the form

$$\log K = A_1 + A_2 \overline{\Delta B_z}, \quad (4)$$

584 where A_1 and A_2 are obtained from the fit line shown in Figures 5 and 6. From this we
585 obtain a corrected value K^* , which estimates the value K would have in the absence of
586 B_z errors, and is given by

$$K^* = K \exp(-A_2 \overline{\Delta B_z}). \quad (5)$$

587 The lower half of Table 1 shows statistics for K^* . As with the K results, data are
588 shown for the SWMF simulations, empirical models, and both together. Each is further
589 broken down into results for the HL and LL IB observations. For K^* , the y axis inter-
590 cept from the fit of equation (4) is also given, along with its 95% confidence interval. The
591 intercepts provide an estimation of what the average value of K would be in the case of
592 zero magnetic field error.

593 From the values in Table 1, it is apparent that the SWMF tends to produce higher
594 values of K (as indicated by the higher median and interquartile ranges) compared with
595 the empirical models. The K^* correction tends to produce smaller values compared with
596 the uncorrected K values, while also reducing the amount of difference between the SWMF
597 and the empirical model results compared with K .

598 The values in Table 1 also show that the LL IB observations tended to be associ-
 599 ated with larger values of K and K^* compared with the HL observations. Each of the
 600 rows of the table showing data from the LL set has a higher median than the correspond-
 601 ing row from the HL set. For instance, the SWMF K estimations for the HL set have
 602 a median of 10.7, while those from the LL set have a median of 11.0. Similarly, the em-
 603 pirical model estimations for the HL set have a median of 10.8, while those for the LL
 604 set have a median of 14.3. This is consistent with the expected relationship between K
 605 and latitude discussed earlier.

606 The $K = 8$ and $K = 13$ percentiles in Table 1 provide an estimate of what frac-
 607 tion of the IB observations might have been produced by current sheet scattering (for
 608 which $K \lesssim 8-13$ is expected). The remaining IB observations (those for which $K \gtrsim$
 609 $8-13$) could potentially be the result of EMIC wave interactions. For SWMF, 23.6% of
 610 the uncorrected HL K values fall below $K = 8$, and 38.6% fall below $K = 13$; for the
 611 LL set it is 20.1% and 35.1%. For the empirical models 40.2% of the values from the HL
 612 set are below $K = 8$ and 61.4% are below $K = 13$, while for the LL set it is 31.5%
 613 and 52.7%. The K^* correction increases the number of SWMF estimates that fall be-
 614 low the $K = 8$ and $K = 13$ thresholds, to 29.1% and 51.6%, respectively, for the HL
 615 set, and 23.3% and 42.2%, respectively, for the LL set. The K^* correction has a some-
 616 what less significant effect on the empirical model results, with the percentages below
 617 the $K = 8$ and $K = 13$ falling within 5% compared with the uncorrected K .

618 Figure 7 shows the distributions of K before and after correction, represented us-
 619 ing kernel density estimation (KDE, Parzen, 1962). A KDE approximates a PDF by con-
 620 volving a set of discrete points with a Gaussian kernel. The resulting plot can be inter-
 621 preted in much the same way as a normalized histogram. The high-latitude (HL) IB data
 622 is shown in blue, and low-latitude (LL) IB data is shown in orange. Figure 7a shows the
 623 distribution of K values estimated by SWMF, while Figure 7b shows the correspond-
 624 ing distribution of K^* . Figures 7c and 7d show K and K^* for the empirical models, while
 625 Figures 7e and 7f show the results of combining the SWMF and empirical results into
 626 a single data set and computing K^* for the combined data set.

631 The empirical models (Figure 7c) produce slightly narrower distributions of K com-
 632 pared with SWMF (Figure 7a), but after correction the distributions become more com-
 633 parable, and the SWMF distribution of K^* for the HL set (Figure 7b) is slightly nar-

627 **Figure 7.** Distributions of (a) K and (b) K^* for all three MHD simulations, and distributions
 628 of (c) K and (d) K^* for all empirical models. (e) and (f) show SWMF and empirical models to-
 629 gether. The distributions have been separated according to whether the observations came from
 630 the high-latitude (HL) or the low-latitude (LL) edge of the IB.

634 rower than that of the empirical models (Figure 7d). For both classes of models, the K^*
 635 correction (Figures 7b, 7d, and 7f) produces a narrower distribution for the HL set com-
 636 pared with the uncorrected K values (Figures 7a, 7c, and 7e). However, for the LL set
 637 the opposite is true, with the SWMF distribution being relatively unaffected and the em-
 638 pirical distribution being widened appreciably. In all the distributions of Figure 7, a no-
 639 ticeable difference can be seen between the LL and HL data. For values of K and K^*
 640 greater than about 20, the probability density is higher for the LL set than for the HL
 641 set, while for values less than this, the probability density is higher for the HL set than
 642 for the LL set. This means that the LL points tend to be associated with higher values
 643 of K . This is consistent with the tendency previously noted in Table 1. When the K^*
 644 correction (Figures 7b, 7d, and 7f) is applied, the same pattern is seen that LL obser-
 645 vations are associated with higher values, and the effect is more pronounced for the cor-
 646 rected values.

647 8 Discussion

648 The goal of this study is to test what fraction of observed IB's during the storm
 649 on 4-6 April 2010 may have been the result of CSS. To accomplish this, we estimated
 650 $K = \frac{R_c}{r_g}$ associated with ion isotropic boundary observations. K provides a measure
 651 of the effectiveness of the CSS process at a particular location. We used MHD and em-
 652 pirical models to trace field lines from the IB observation locations to the magnetotail,
 653 and to estimate K where those field lines cross the current sheet. We then corrected our
 654 K estimations for errors in the model magnetic fields that could be quantified with in
 655 situ observations from spacecraft in the magnetotail. By correcting for these errors, and
 656 by using of multiple models to estimate K , we are able to constrain the possible range
 657 of K . This is the first study to explore IB properties using an MHD model during storm
 658 conditions.

659 A number of previous studies have noted a tendency for SWMF to produce under-
660 stretched magnetic fields on the night side. As discussed in section 5, this is expected
661 to result in overestimation of K . Glocer et al. (2009) found that SWMF overestimated
662 B_z at GOES spacecraft during a storms on 4 May 1998 and 31 March 2001, though they
663 also found that this could be improved by coupling a wind model to BATS-R-US. Ganushk-
664 ina, Liemohn, Kubyshkina, Ilie, and Singer (2010) showed that SWMF overestimated
665 B_z at GOES spacecraft during storms on 6–7 November, 1997 and 21–23 October, 1998.
666 Ilie et al. (2015) reported over-prediction at GOES, Geotail, and THEMIS spacecraft dur-
667 ing a quiet interval on 13 February, 2009, and Haiducek et al. (2019 *accepted*) reported
668 this for different simulations of the same event. In the present study we find this ten-
669 dency as well, with all three simulations overestimating B_z for about 65–70% of the IB
670 observations.

671 The amount of tail stretching in TA16 was previously reported to be similar to the
672 older T89 model (Tsyganenko & Andreeva, 2016), which in turn has been reported as
673 producing overstretched fields in the magnetotail (Peredo, Stern, & Tsyganenko, 1993;
674 Tsyganenko, 1989). Haiducek et al. (2019 *accepted*) reported understretched fields for
675 T01 and overstretched fields in TS05 and TA16. Results in the present work show a slight
676 tendency toward over-stretching in T01, but a slight tendency toward under-stretching
677 in TS05 and TA16, based on errors in B_z relative to in situ observations.

678 Compared with SWMF, the empirical models tend to produce smaller values of K ,
679 consistent with the tendency noted above of understretched fields in SWMF and over-
680 stretched fields in the empirical models. However, the distributions of K overlap signif-
681 icantly between the two classes of models even before correction. The median K values
682 and percentiles in Table 1 demonstrate that, after correction, the difference between the
683 distributions of K obtained using MHD and those obtained using the empirical models
684 is less than the difference between the K distributions found by using different criteria
685 of IB selection (HL or LL data sets). This is different from the quiet time results of Haiducek
686 et al. (2019 *accepted*), which included non-overlapping distributions of uncorrected K ,
687 with the empirical models tending toward quite small values of K and the SWMF K val-
688 ues uniformly above 10. The overlapping distributions reflect the presence of much higher
689 K estimates (on average) coming from the empirical models compared with Haiducek
690 et al. (2019 *accepted*), along with marginally lower K estimates from SWMF and broader
691 distributions for both classes of models. The broader distributions are probably the re-

692 result of using less restrictive selection criteria for the IB observations, as well as storm-
 693 time variability. Storm conditions likely increase the range of K estimates both by caus-
 694 ing the true value of K to vary more broadly (due to EMIC scattering, as well as pro-
 695 ducing CSS under a wider variety of conditions). Storm conditions also create rapidly
 696 varying dynamics which the models are not always able to reproduce, contributing to
 697 errors in magnetic field configuration and causing randomly varying errors in K .

698 The results of our study are somewhat different from those obtained by Dubyagin
 699 et al. (2018) using the TS05 model in the 21–03 MLT sector for larger statistics (nine
 700 storms, > 200 IB observations). Dubyagin et al. (2018) found that 68% of the events
 701 in their HL data set had $K^* < 13$, which is reasonably close to the 66.1% obtained from
 702 the HL data set using empirical models in our study. However, 63% of their LL IB's had
 703 $K^* < 13$, which is significantly higher than the 51.3% in our LL data set (see Table 1).
 704 In both cases the percentages are lower. When the SWMF results are added, the per-
 705 centages decrease further since SWMF tends to produce higher values for K and K^* .
 706 Finally using a $K^* < 8$ threshold condition reduces the percentages further. The lower
 707 percentages we obtained compared to Dubyagin et al. (2018) can be attributed to sev-
 708 eral factors including

- 709 • A different methodology for estimating the uncertainty (the use of two K thresh-
 710 olds versus a single one)
- 711 • The use of multiple models (three empirical models, plus three MHD simulations)
 712 in the present work, compared with a single empirical model in Dubyagin et al.
 713 (2018)
- 714 • The application of additional restrictions on MLT and ΔB_z by Dubyagin et al.
 715 (2018)
- 716 • Differences in the magnetospheric state between the storm we analyzed and those
 717 analyzed in Dubyagin et al. (2018)

718 Given the differences in the analysis, and in the events included in the two stud-
 719 ies, our paper and Dubyagin et al. (2018) should be considered complementary, but some
 720 caution should be applied when making quantitative comparisons between the two.

721 The results in Haiducek et al. (2019 *accepted*) made it clear that errors in the mag-
 722 netic field models can affect K values significantly, but also that such errors, if quanti-

723 fied, can be corrected for effectively. However, it should be noted that the corrections
724 provide only a rough estimate of the true value of K . These corrections are subject to
725 a number of sources of uncertainty, including errors due to the linearization of the ex-
726 pression for K , the position of satellites relative to where K is actually estimated, and
727 the fact that our correction procedure involves a fit to numerous K estimates from nu-
728 merous IB observations, each of which came from a different time, with a different mag-
729 netospheric state and different satellite positions for each. By fitting all of these points
730 together we find the average relationship between the magnetic field errors and K es-
731 timates. The true relationship between the two probably varies with the magnetospheric
732 state and the satellite positions, which our correction procedure does not account for.
733 With the ΔB_z estimates there is a potential issue with the GOES magnetometer data
734 in that it may contain offsets of unknown magnitude (Singer et al., 1996).

735 Despite these sources of uncertainty, there are indications that the correction pro-
736 cedure is successful in removing much of the difference between the two classes of mod-
737 els. The distributions of K become narrower and substantially more similar to each other
738 after correction. While we have no ground-truth measurement with which to test our
739 K estimations, we interpret the similarity between the distributions of K obtained by
740 very different types of models as a sign that both are likely reproducing the major char-
741 acteristics of the true K distribution. On the other hand, we also noted in section 7 that
742 the correction procedure seems to amplify the differences between the HL and LL data
743 sets. This is largely due to the correction procedure narrowing the distribution of K ob-
744 tained from the HL IB observations, while the distribution of K derived from the LL data
745 is relatively unchanged. This could indicate that the LL data are subject to greater in-
746 accuracies in the ΔB_z estimates used in the correction, or that the LL data are more sen-
747 sitive to additional error terms not included in the correction procedure. Another pos-
748 sibility is that variance in the incident particle population prior to scattering plays a greater
749 role for the particles observed at the LL latitudes. Finally, it is possible that the pro-
750 cedure used to identify the HL and LL locations is somehow more precise for the HL lat-
751 itudes.

752 In addition to checking the K values to determine whether they are below a given
753 threshold value, we can also check for a dependence on MLT as an indication of whether
754 CSS is the mechanism responsible for IB formation. EMIC scattering has been noted to
755 contribute significantly to proton precipitation in the dusk sector (e.g. Fuselier, 2004; Yah-

784 **Figure 8.** (a) HL IB latitude as a function of MLT, (b) LL IB latitude as a function of MLT,
 785 (c) HL K^* as a function of MLT, (d) LL K^* as a function of MLT. All points are colored by
 786 $Symh-H^*$. Shapes in (c) and (d) denote the class of model (SWMF or empirical).

756 nin & Yahnina, 2007; Zhang, Paxton, & Zheng, 2008). A number of previous studies have
 757 found a noon-midnight asymmetry in IB latitude, characterized by a night side minimum
 758 latitude and a day side maximum latitude (e.g. Asikainen et al., 2010; Ganushkina et
 759 al., 2005; V. A. Sergeev et al., 1993; Yue et al., 2014). In addition, many studies have
 760 found a tendency for IB latitude to decrease as $Symh-H$ becomes more negative (e.g.
 761 Asikainen et al., 2010; Dubyagin et al., 2018; Ganushkina et al., 2005; Hauge & S oraas,
 762 1975; Lvova et al., 2005; S oraas et al., 2002). In most cases the noon-midnight asymme-
 763 try in latitude is accompanied by a weaker dawn-dusk asymmetry, with the minimum
 764 IB latitude occurring around 23 MLT (e.g. Asikainen et al., 2010; Ganushkina et al., 2005;
 765 Lvova et al., 2005; Newell et al., 1998; V. A. Sergeev, Bikkuzina, & Newell, 1997; Yue
 766 et al., 2014). Figures 8a and 8b show the latitude of our IB observations as a function
 767 of MLT, with the HL data set shown in Figure 8a and the LL data set in 8b. As has been
 768 seen by previous authors, the minimum IB latitude occurs in the pre-midnight sector,
 769 and a dawn-dusk asymmetry is clearly visible. A correlation with $Symh-H$ is also ap-
 770 parent. Figures 8c and 8d show K^* as a function of MLT, with the HL data in Figure 8c
 771 and the LL data in Figure 8d. All plots of Figure 8 are colored by $Symh-H^*$, and SWMF
 772 results are plotted with triangles while empirical models are plotted with squares. Fig-
 773 ure 8 shows that K^* exhibits none of the trends found in the IB latitude, which is con-
 774 sistent with CSS playing a significant role in IB formation since it suggests that K is con-
 775 trolling the pitch angle scattering rather than some other process. Note however that
 776 the MLT dependence shown in Figure 8 is affected by the motions of the GOES and THEMIS
 777 satellites since we use only IB observations that are conjugate with those spacecraft. It
 778 should be noted that independence of the K parameter on MLT was also found by Dubya-
 779 gin et al. (2018) using only empirical models. However, that study concentrated on a nar-
 780 rower MLT sector (21–03 MLT), and there were serious doubts that this dependence would
 781 not emerge if 18–21 MLT sector was included. Indeed, the plasmaspheric plume is of-
 782 ten seen at ≈ 18 MLT and the EMIC wave related precipitations have also been detected
 783 in this sector (Yahnin & Yahnina, 2007).

787 The independence of K^* on MLT, despite a dependence of IB latitude on MLT,
788 was interpreted by Dubyagin et al. (2018) as an indication that the CSS was the oper-
789 ative scattering mechanism for a majority of their data. Our results also find K^* to be
790 independent of MLT, even though a lower percentage of our K^* values were within the
791 expected range for CSS. We conducted additional tests in which we plotted K^* as a func-
792 tion of MLT while limiting the data set to IB observations for which K^* exceeded a spec-
793 ified threshold. By doing so we found that K^* is independent of MLT even when $K^* >$
794 30. This could indicate that the lack of dependence of K^* is not due to K controlling
795 the scattering process, but is simply the result of random variations in the estimated K
796 values due to mapping errors which are large enough to obscure the MLT dependence.
797 If this is the case, then the mapping accuracy must be increased before the dependence
798 of K on MLT can be used reliably as an indicator of CSS, and comparison of K with
799 a threshold value is probably the better criterion.

800 The conclusions of the paper can be summarized as follows:

- 801 1. By correcting each K estimate using in situ observations from 2–3 conjugate satel-
802 lites in the current sheet, we were able to produce consistent results, with simi-
803 lar distributions of K obtained using both empirical and MHD models.
- 804 2. Accounting for uncertainty in the IB latitude and in the threshold condition for
805 K , we find that between 29% and 54% of the IB observations may be the result
806 of CSS.
- 807 3. We find that K^* is independent of both $Symb-H^*$ and MLT during this storm
808 interval, and this independence persists even for high K values.

809 Acknowledgments

810 The NOAA/POES particle data were downloaded from the National Geophysical
811 Data Center website: <https://www.ngdc.noaa.gov/stp/satellite/poes/index.html>.

812 Thanks to Howard Singer for providing the GOES magnetometer data. The mag-
813 netometer data (in spacecraft coordinates) can be found online at [https://satdat.ngdc](https://satdat.ngdc.noaa.gov/sem/goes/data/avg/)
814 [.noaa.gov/sem/goes/data/avg/](https://satdat.ngdc.noaa.gov/sem/goes/data/avg/). GOES magnetometer data in GSM coordinates is in-
815 cluded in the supporting information.

816 THEMIS data were retrieved using the THEMIS Data Analysis Software (TDAS;
817 <http://themis.igpp.ucla.edu/software.shtml>). We acknowledge NASA contract
818 NAS5-02099 and V. Angelopoulos for use of data from the THEMIS Mission. Specifi-
819 cally: K. H. Glassmeier, U. Auster and W. Baumjohann for the use of FGM data pro-
820 vided under the lead of the Technical University of Braunschweig and with financial sup-
821 port through the German Ministry for Economy and Technology and the German Cen-
822 ter for Aviation and Space (DLR) under contract 50 OC 0302, and C. W. Carlson and
823 J. P. McFadden for use of ESA data.

824 The research of S. Dubyagin and N. Ganushkina leading to these results was partly
825 funded by the European Union's Horizon 2020 research and innovation programme un-
826 der grant agreement 637302 PROGRESS. The work at the University of Michigan was
827 also partly funded by the National Aeronautics and Space Administration under grant
828 agreements NNX14AF34G, NNX17AB87G and 80NSS17K0015 issued through the ROSES-
829 2013 and ROSES-2016 programmes and by the National Science Foundation under grant
830 agreement 1663770.

831 Part of the results presented here has been achieved under the framework of the
832 Finnish Centre of Excellence in Research of Sustainable Space (FORESAIL) funded by
833 the Academy of Finland, decision number 312351.

834 Portions of the work of J. Haiducek leading to these results were performed while
835 he held a National Research Council (NRC) Research Associateship award at the U.S.
836 Naval Research Laboratory.

837 Portions of the work of J. Haiducek leading to these results were financially sup-
838 ported by the U.S. Veterans administration under the Post-9/11 GI Bill.

839 The Spacepy python library (Burrell et al., 2018; Morley, Koller, Welling, Larsen,
840 & Niehof, 2014; Morley et al., 2011) was used for a number of tasks related to reading
841 and analyzing data in this paper.

842 References

843 Alfvén, H., & Fälthammar, C. G. (1963). *Cosmical electrodynamics: Fundamen-*
844 *tal Principles (Volume 1)*. Clarendon Press. Retrieved from [https://books](https://books.google.com/books?id=3aIEAQAIAAJ)
845 [.google.com/books?id=3aIEAQAIAAJ](https://books.google.com/books?id=3aIEAQAIAAJ)

- 846 Asikainen, T., Maliniemi, V., & Mursula, K. (2010, dec). Modeling the contributions
847 of ring, tail, and magnetopause currents to the corrected Dst index. *Journal of*
848 *Geophysical Research: Space Physics*, 115(A12). Retrieved from [http://doi](http://doi.wiley.com/10.1029/2010JA015774)
849 [.wiley.com/10.1029/2010JA015774](http://doi.wiley.com/10.1029/2010JA015774) doi: 10.1029/2010JA015774
- 850 Asikainen, T., Mursula, K., & Maliniemi, V. (2012, sep). Correction of de-
851 tector noise and recalibration of NOAA/MEPED energetic proton fluxes.
852 *Journal of Geophysical Research: Space Physics*, 117(A9), A09204. Re-
853 trieved from <http://doi.wiley.com/10.1029/2012JA017593> doi:
854 10.1029/2012JA017593
- 855 Auster, H. U., Glassmeier, K. H., Magnes, W., Aydogar, O., Baumjohann, W.,
856 Constantinescu, D., ... Wiedemann, M. (2008, dec). The THEMIS Flux-
857 gate Magnetometer. *Space Science Reviews*, 141(1-4), 235–264. Retrieved
858 from <http://link.springer.com/10.1007/s11214-008-9365-9> doi:
859 10.1007/s11214-008-9365-9
- 860 Baker, K. B., & Wing, S. (1989, jul). A new magnetic coordinate system for conju-
861 gate studies at high latitudes. *Journal of Geophysical Research: Space Physics*,
862 94(A7), 9139–9143. Retrieved from [http://onlinelibrary.wiley.com/doi/](http://onlinelibrary.wiley.com/doi/10.1029/JA094iA07p09139/abstract)
863 [10.1029/JA094iA07p09139/abstract](http://onlinelibrary.wiley.com/doi/10.1029/JA094iA07p09139/abstract) doi: 10.1029/JA094iA07p09139
- 864 Brambles, O. J., Lotko, W., Zhang, B., Ouellette, J., Lyon, J., & Wiltberger, M.
865 (2013, oct). The effects of ionospheric outflow on ICME and SIR driven
866 sawtooth events. *Journal of Geophysical Research: Space Physics*, 118(10),
867 6026–6041. Retrieved from [https://agupubs.onlinelibrary.wiley.com/](https://agupubs.onlinelibrary.wiley.com/doi/abs/10.1002/jgra.50522)
868 [doi/abs/10.1002/jgra.50522](https://agupubs.onlinelibrary.wiley.com/doi/abs/10.1002/jgra.50522) doi: 10.1002/JGRA.50522
- 869 Brambles, O. J., Lotko, W., Zhang, B., Wiltberger, M., Lyon, J., & Strange-
870 way, R. J. (2011, jun). Magnetosphere Sawtooth Oscillations Induced
871 by Ionospheric Outflow. *Science*, 332(6034), 1183–1186. Retrieved from
872 <http://www.sciencemag.org/cgi/doi/10.1126/science.1202869> doi:
873 10.1126/science.1202869
- 874 Büchner, J., & Zelenyi, L. M. (1987, dec). Chaotization of the electron motion as
875 the cause of an internal magnetotail instability and substorm onset. *Journal*
876 *of Geophysical Research*, 92(A12), 13456–13466. Retrieved from [http://doi](http://doi.wiley.com/10.1029/JA092iA12p13456)
877 [.wiley.com/10.1029/JA092iA12p13456](http://doi.wiley.com/10.1029/JA092iA12p13456) doi: 10.1029/JA092iA12p13456
- 878 Burrell, A. G., Halford, A. J., Klenzing, J., Stoneback, R. A., Morley, S. K., Annex,

- 879 A. M., ... Ma, J. (2018, November). Snakes on a Spaceship - An Overview of
880 Python in Heliophysics. *Journal of Geophysical Research: Space Physics*. doi:
881 10.1029/2018JA025877
- 882 Burton, R. K., McPherron, R. L., & Russell, C. T. (1975, nov). An empirical
883 relationship between interplanetary conditions and Dst. *Journal of Geophys-*
884 *ical Research*, 80(31), 4204–4214. Retrieved from [http://doi.wiley.com/](http://doi.wiley.com/10.1029/JA080i031p04204)
885 10.1029/JA080i031p04204 doi: 10.1029/JA080i031p04204
- 886 Daglis, I. A. (1997). The role of magnetosphere-ionosphere coupling in magnetic
887 storm dynamics. In *Magnetic storms* (pp. 107–116). American Geophysical
888 Union (AGU). Retrieved from <http://doi.wiley.com/10.1029/GM098p0107>
889 doi: 10.1029/GM098p0107
- 890 Delcourt, D. C., Malova, H. V., & Zelenyi, L. M. (2006). Quasi-adiabaticity in
891 bifurcated current sheets. *Geophysical Research Letters*, 33(6), L06106.
892 Retrieved from [https://agupubs.onlinelibrary.wiley.com/doi/pdf/](https://agupubs.onlinelibrary.wiley.com/doi/pdf/10.1029/2005GL025463)
893 10.1029/2005GL025463 doi: 10.1029/2005GL025463
- 894 Delcourt, D. C., Moore, T. E., Giles, B. L., & Fok, M.-C. (2000, nov). Quan-
895 titative modeling of modulated ion injections observed by Polar-Thermal
896 Ion Dynamics Experiment in the cusp region. *Journal of Geophysical Re-*
897 *search: Space Physics*, 105(A11), 25191–25203. Retrieved from [https://](https://agupubs.onlinelibrary.wiley.com/doi/pdf/10.1029/2000JA000034)
898 agupubs.onlinelibrary.wiley.com/doi/pdf/10.1029/2000JA000034 doi:
899 10.1029/2000JA000034
- 900 Delcourt, D. C., Sauvaud, J.-A., Martin, R. F., & Moore, T. E. (1996, aug). On
901 the nonadiabatic precipitation of ions from the near-Earth plasma sheet. *Jour-*
902 *nal of Geophysical Research: Space Physics*, 101(A8), 17409–17418. Retrieved
903 from <http://doi.wiley.com/10.1029/96JA01006> doi: 10.1029/96JA01006
- 904 DeZeeuw, D. L., Gombosi, T. I., Groth, C. P. T., Powell, K. G., & Stout, Q. F.
905 (2000). An Adaptive MHD Method for Global Space Weather Simulations.
906 *IEEE Trans. Plasma Sci.*, 28(6), 1956-1965. doi: 10.1109/27.902224
- 907 Dubyagin, S., Ganushkina, N., Apatenkov, S., Kubyshkina, M., Singer, H., &
908 Liemohn, M. (2013, mar). Geometry of duskside equatorial current during
909 magnetic storm main phase as deduced from magnetospheric and low-altitude
910 observations. *Annales Geophysicae*, 31(3), 395–408. Retrieved from [http://](http://www.ann-geophys.net/31/395/2013/)
911 www.ann-geophys.net/31/395/2013/ doi: 10.5194/angeo-31-395-2013

- 912 Dubyagin, S., Ganushkina, N. Y., & Sergeev, V. (2018, may). Formation of 30 KeV
 913 Proton Isotropic Boundaries During Geomagnetic Storms. *Journal of Geo-*
 914 *physical Research: Space Physics*. Retrieved from [http://doi.wiley.com/](http://doi.wiley.com/10.1002/2017JA024587)
 915 [10.1002/2017JA024587](http://doi.wiley.com/10.1002/2017JA024587) doi: 10.1002/2017JA024587
- 916 Erlandson, R. E., & Ukhorskiy, A. J. (2001, March). Observations of electromag-
 917 netic ion cyclotron waves during geomagnetic storms: Wave occurrence and
 918 pitch angle scattering. , *106*(A3). doi: 10.1029/2000JA000083
- 919 Evans, D. S., & Greer, M. S. (2000). *Polar Orbiting Environmental Satellite Space*
 920 *Environment Monitor -2 Instrument Descriptions and Archive Data Documen-*
 921 *tation* (Tech. Rep.). Boulder, Colorado: National Oceanic and Atmospheric
 922 Administration. Retrieved from [ftp://satdat.ngdc.noaa.gov/sem/poes/](ftp://satdat.ngdc.noaa.gov/sem/poes/docs/sem2_docs/2006/SEM2v2.0.pdf)
 923 [docs/sem2_docs/2006/SEM2v2.0.pdf](ftp://satdat.ngdc.noaa.gov/sem/poes/docs/sem2_docs/2006/SEM2v2.0.pdf)
- 924 Fuselier, S. A. (2004). Generation of transient dayside subauroral proton pre-
 925 cipitation. *Journal of Geophysical Research*, *109*(A12), A12227. Re-
 926 trieved from <http://doi.wiley.com/10.1029/2004JA010393> doi:
 927 [10.1029/2004JA010393](http://doi.wiley.com/10.1029/2004JA010393)
- 928 Ganushkina, N. Y., Liemohn, M. W., Kubyshkina, M. V., Ilie, R., & Singer,
 929 H. J. (2010, jan). Distortions of the magnetic field by storm-time cur-
 930 rent systems in Earth's magnetosphere. *Annales Geophysicae*, *28*(1), 123-
 931 140. Retrieved from <http://www.ann-geophys.net/28/123/2010/> doi:
 932 [10.5194/angeo-28-123-2010](http://www.ann-geophys.net/28/123/2010/)
- 933 Ganushkina, N. Y., Pulkkinen, T. I., Kubyshkina, M. V., Sergeev, V. A., Lvova,
 934 E. A., Yahnina, T. A., ... Fritz, T. (2005, jul). Proton isotropy boundaries
 935 as measured on mid- and low-altitude satellites. *Annales Geophysicae*, *23*(5),
 936 1839-1847. Retrieved from <http://www.ann-geophys.net/23/1839/2005/>
 937 doi: 10.5194/angeo-23-1839-2005
- 938 Gilson, M. L., Raeder, J., Donovan, E., Ge, Y. S., & Kepko, L. (2012, may).
 939 Global simulation of proton precipitation due to field line curvature dur-
 940 ing substorms. *Journal of Geophysical Research: Space Physics*, *117*(A5),
 941 A05216. Retrieved from <http://doi.wiley.com/10.1029/2012JA017562> doi:
 942 [10.1029/2012JA017562](http://doi.wiley.com/10.1029/2012JA017562)
- 943 Glocer, A., Tóth, G., Gombosi, T., & Welling, D. (2009, may). Modeling
 944 ionospheric outflows and their impact on the magnetosphere, initial re-

- 945 sults. *Journal of Geophysical Research: Space Physics*, 114(A5), n/a–n/a.
 946 Retrieved from <http://doi.wiley.com/10.1029/2009JA014053> doi:
 947 10.1029/2009JA014053
- 948 Gvozdevsky, B. B., Sergeev, V. A., & Mursula, K. (1997, nov). Long lasting en-
 949 ergetic proton precipitation in the inner magnetosphere after substorms. *Jour-*
 950 *nal of Geophysical Research: Space Physics*, 102(A11), 24333–24338. Retrieved
 951 from <http://doi.wiley.com/10.1029/97JA02062> doi: 10.1029/97JA02062
- 952 Haiducek, J. D., Ganushkina, N. Y., Dubyagin, S., & Welling, D. T. (2019 *accepted*).
 953 Relating observed locations of energetic proton isotropic boundaries with mag-
 954 netic field geometry during quiet times. *Journal of Geophysical Research:*
 955 *Space Physics*.
- 956 Haiducek, J. D., Welling, D. T., Ganushkina, N. Y., Morley, S. K., & Ozturk, D. S.
 957 (2017, dec). SWMF Global Magnetosphere Simulations of January 2005: Ge-
 958 omagnetic Indices and Cross-Polar Cap Potential. *Space Weather*, 15(12),
 959 1567–1587. Retrieved from <http://doi.wiley.com/10.1002/2017SW001695>
 960 doi: 10.1002/2017SW001695
- 961 Halford, A. J., Fraser, B. J., & Morley, S. K. (2010, dec). EMIC wave activity dur-
 962 ing geomagnetic storm and nonstorm periods: CRRES results. *Journal of Geo-*
 963 *physical Research: Space Physics*, 115(A12), A12248. Retrieved from [http://](http://doi.wiley.com/10.1029/2010JA015716)
 964 doi.wiley.com/10.1029/2010JA015716 doi: 10.1029/2010JA015716
- 965 Hauge, R., & Söraas, F. (1975, aug). Precipitation of > 115 keV protons in the
 966 evening and forenoon sectors in relation to the magnetic activity. *Plan-*
 967 *etary and Space Science*, 23(8), 1141–1154. Retrieved from [https://](https://www.sciencedirect.com/science/article/pii/0032063375901646)
 968 www.sciencedirect.com/science/article/pii/0032063375901646 doi:
 969 10.1016/0032-0633(75)90164-6
- 970 Ilie, R., Ganushkina, N., Toth, G., Dubyagin, S., & Liemohn, M. W. (2015,
 971 dec). Testing the magnetotail configuration based on observations of low-
 972 altitude isotropic boundaries during quiet times. *Journal of Geophysical*
 973 *Research: Space Physics*, 120(12), 10,557–10,573. Retrieved from [http://](http://doi.wiley.com/10.1002/2015JA021858)
 974 doi.wiley.com/10.1002/2015JA021858 doi: 10.1002/2015JA021858
- 975 Imhof, W. L., Reagan, J. B., & Gaines, E. E. (1977, nov). Fine-scale spatial struc-
 976 ture in the pitch angle distributions of energetic particles near the midnight
 977 trapping boundary. *Journal of Geophysical Research*, 82(32), 5215–5221.

- 978 Retrieved from <http://doi.wiley.com/10.1029/JA082i032p05215> doi:
979 10.1029/JA082i032p05215
- 980 Kennel, C. F., & Petschek, H. E. (1966, jan). Limit on stably trapped particle
981 fluxes. *Journal of Geophysical Research*, 71(1), 1–28. Retrieved from [http://](http://doi.wiley.com/10.1029/JZ071i001p00001)
982 doi.wiley.com/10.1029/JZ071i001p00001 doi: 10.1029/JZ071i001p00001
- 983 Liang, J., Donovan, E., Ni, B., Yue, C., Jiang, F., & Angelopoulos, V. (2014, oct).
984 On an energy-latitude dispersion pattern of ion precipitation potentially as-
985 sociated with magnetospheric EMIC waves. *Journal of Geophysical Research:*
986 *Space Physics*, 119(10), 8137–8160. Retrieved from [http://doi.wiley.com/](http://doi.wiley.com/10.1002/2014JA020226)
987 [10.1002/2014JA020226](http://doi.wiley.com/10.1002/2014JA020226) doi: 10.1002/2014JA020226
- 988 Liu, Y., Luhmann, J. G., Bale, S. D., & Lin, R. P. (2011, jun). Solar source
989 and heliospheric consequences of the 2010 April 3 coronal mass ejection: A
990 comprehensive view. *The Astrophysical Journal*, 734(2), 84. Retrieved
991 from <http://stacks.iop.org/0004-637X/734/i=2/a=84?key=crossref>
992 [.2176f4318b7aa8cf7c81e1bf22b1f69d](http://stacks.iop.org/0004-637X/734/i=2/a=84?key=crossref) doi: 10.1088/0004-637X/734/2/84
- 993 Lvova, E. A., Sergeev, V. A., & Bagautdinova, G. R. (2005). Statistical study of
994 the proton isotropy boundary. *Annales Geophysicae*, 23, 1311–1316. Re-
995 trieved from [https://hal-insu.archives-ouvertes.fr/file/index/docid/](https://hal-insu.archives-ouvertes.fr/file/index/docid/317716/filename/angeo-23-1311-2005.pdf)
996 [317716/filename/angeo-23-1311-2005.pdf](https://hal-insu.archives-ouvertes.fr/file/index/docid/317716/filename/angeo-23-1311-2005.pdf)
- 997 McFadden, J. P., Carlson, C. W., Larson, D., Bonnell, J., Mozer, F., Angelopou-
998 los, V., ... Auster, U. (2008, dec). THEMIS ESA First Science Results
999 and Performance Issues. *Space Science Reviews*, 141(1-4), 477–508. Re-
1000 trieved from <http://link.springer.com/10.1007/s11214-008-9433-1> doi:
1001 [10.1007/s11214-008-9433-1](http://link.springer.com/10.1007/s11214-008-9433-1)
- 1002 McFadden, J. P., Carlson, C. W., Larson, D., Ludlam, M., Abiad, R., Elliott, B.,
1003 ... Angelopoulos, V. (2008, dec). The THEMIS ESA Plasma Instrument
1004 and In-flight Calibration. *Space Science Reviews*, 141(1-4), 277–302. Re-
1005 trieved from <http://link.springer.com/10.1007/s11214-008-9440-2> doi:
1006 [10.1007/s11214-008-9440-2](http://link.springer.com/10.1007/s11214-008-9440-2)
- 1007 Meurant, M., Gérard, J.-C., Blockx, C., Spanswick, E., Donovan, E. F., Hubert,
1008 B., ... Connors, M. (2007, may). EL - a possible indicator to monitor the
1009 magnetic field stretching at global scale during substorm expansive phase:
1010 Statistical study. *Journal of Geophysical Research: Space Physics*, 112(A5),

- 1011 A05222. Retrieved from <http://doi.wiley.com/10.1029/2006JA012126> doi:
1012 10.1029/2006JA012126
- 1013 Morley, S., Koller, J., Welling, D., Larsen, B., & Niehof, J. (2014, January).
1014 *SpacePy: Python-Based Tools for the Space Science Community*. Astrophysics
1015 Source Code Library.
- 1016 Morley, S. K., Welling, D. T., Koller, J., Larsen, B. A., Henderson, M. G., & Niehof,
1017 J. (2011). SpacePy - A Python-based Library of Tools for the Space Sci-
1018 ences. *Proceedings of the 9th Python in Science Conference*, 39–45. Re-
1019 trieved from [https://conference.scipy.org/proceedings/scipy2010/](https://conference.scipy.org/proceedings/scipy2010/pdfs/morley.pdf)
1020 [pdfs/morley.pdf](https://conference.scipy.org/proceedings/scipy2010/pdfs/morley.pdf)
- 1021 Möstl, C., Temmer, M., Rollett, T., Farrugia, C. J., Liu, Y., Veronig, A. M., ...
1022 Biernat, H. K. (2010, dec). STEREO and Wind observations of a fast ICME
1023 flank triggering a prolonged geomagnetic storm on 5-7 April 2010. *Geophysical*
1024 *Research Letters*, 37(24), n/a–n/a. Retrieved from [http://doi.wiley.com/](http://doi.wiley.com/10.1029/2010GL045175)
1025 [10.1029/2010GL045175](http://doi.wiley.com/10.1029/2010GL045175) doi: 10.1029/2010GL045175
- 1026 Newell, P. T., Sergeev, V. A., Bikkuzina, G. R., & Wing, S. (1998, mar). Char-
1027 acterizing the state of the magnetosphere: Testing the ion precipitation
1028 maxima latitude (b2i) and the ion isotropy boundary. *Journal of Geo-*
1029 *physical Research: Space Physics*, 103(A3), 4739–4745. Retrieved from
1030 <http://doi.wiley.com/10.1029/97JA03622> doi: 10.1029/97JA03622
- 1031 Newell, P. T., Sotirelis, T., Liou, K., Meng, C.-I., & Rich, F. J. (2007, jan). A nearly
1032 universal solar wind-magnetosphere coupling function inferred from 10 mag-
1033 netospheric state variables. *Journal of Geophysical Research: Space Physics*,
1034 112(A1). Retrieved from <http://doi.wiley.com/10.1029/2006JA012015>
1035 doi: 10.1029/2006JA012015
- 1036 Parzen, E. (1962, 09). On estimation of a probability density function and mode.
1037 *Ann. Math. Statist.*, 33(3), 1065–1076. Retrieved from [http://dx.doi.org/10](http://dx.doi.org/10.1214/aoms/1177704472)
1038 [.1214/aoms/1177704472](http://dx.doi.org/10.1214/aoms/1177704472) doi: 10.1214/aoms/1177704472
- 1039 Peredo, M., Stern, D. P., & Tsyganenko, N. A. (1993). Are existing magnetospheric
1040 models excessively stretched? *Journal of Geophysical Research*, 98(A9), 15343.
1041 Retrieved from <http://doi.wiley.com/10.1029/93JA01150> doi: 10.1029/
1042 93JA01150
- 1043 Popova, T. A., Yahnin, A. G., Demekhov, A. G., & Chernyaeva, S. A. (2018, jul).

- 1044 Generation of EMIC Waves in the Magnetosphere and Precipitation of Ener-
 1045 getic Protons: Comparison of the Data from THEMIS High Earth Orbiting
 1046 Satellites and POES Low Earth Orbiting Satellites. *Geomagnetism and Aeron-*
 1047 *omy*, 58(4), 469–482. Retrieved from [http://link.springer.com/10.1134/](http://link.springer.com/10.1134/S0016793218040114)
 1048 [S0016793218040114](http://link.springer.com/10.1134/S0016793218040114) doi: 10.1134/S0016793218040114
- 1049 Powell, K. G., Roe, P. L., Linde, T. J., Gombosi, T. I., & De Zeeuw, D. L. (1999,
 1050 sep). A Solution-Adaptive Upwind Scheme for Ideal Magnetohydrodynam-
 1051 ics. *Journal of Computational Physics*, 154(2), 284–309. Retrieved from
 1052 <http://linkinghub.elsevier.com/retrieve/pii/S002199919996299X> doi:
 1053 10.1006/jcph.1999.6299
- 1054 Ridley, A. J., Gombosi, T. I., & De Zeeuw, D. L. (2004, feb). Ionospheric control of
 1055 the magnetosphere: conductance. *Annales Geophysicae*, 22(2), 567–584. doi:
 1056 10.5194/angeo-22-567-2004
- 1057 Ridley, A. J., & Liemohn, M. W. (2002, aug). A model-derived storm time asym-
 1058 metric ring current driven electric field description. *Journal of Geophysical Re-*
 1059 *search: Space Physics*, 107(A8), SMP 2–1–SMP 2–12. Retrieved from [http://](http://doi.wiley.com/10.1029/2001JA000051)
 1060 doi.wiley.com/10.1029/2001JA000051 doi: 10.1029/2001JA000051
- 1061 Sazykin, S. Y. (2000). *Theoretical Studies of Penetration of Magnetospheric Electric*
 1062 *Fields to the Ionosphere* (Unpublished doctoral dissertation). Utah State Uni-
 1063 versity, Logan, Utah.
- 1064 Sergeev, V., Sazhina, E., Tsyganenko, N., Lundblad, J., & Søråas, F. (1983, oct).
 1065 Pitch-angle scattering of energetic protons in the magnetotail current sheet
 1066 as the dominant source of their isotropic precipitation into the nightside iono-
 1067 sphere. *Planetary and Space Science*, 31(10), 1147–1155. Retrieved from
 1068 <https://www.sciencedirect.com/science/article/pii/0032063383901034>
 1069 doi: 10.1016/0032-0633(83)90103-4
- 1070 Sergeev, V., & Tsyganenko, N. (1982, oct). Energetic particle losses and
 1071 trapping boundaries as deduced from calculations with a realistic mag-
 1072 netic field model. *Planetary and Space Science*, 30(10), 999–1006. doi:
 1073 10.1016/0032-0633(82)90149-0
- 1074 Sergeev, V. A., Bikkuzina, G. R., & Newell, P. T. (1997, September). Dayside
 1075 isotropic precipitation of energetic protons. *Annales Geophysicae*, 15(10),
 1076 1233–1245. doi: 10.1007/s00585-997-1233-5

- 1077 Sergeev, V. A., Chernyaev, I. A., Angelopoulos, V., & Ganushkina, N. Y. (2015,
1078 dec). Magnetospheric conditions near the equatorial footpoints of proton
1079 isotropy boundaries. *Annales Geophysicae*, *33*(12), 1485–1493. Retrieved from <http://www.ann-geophys.net/33/1485/2015/> doi: 10.5194/
1080 angeo-33-1485-2015
- 1081
- 1082 Sergeev, V. A., Chernyaeva, S. A., Apatenkov, S. V., Ganushkina, N. Y., & Dubya-
1083 gin, S. V. (2015, aug). Energy-latitude dispersion patterns near the isotropy
1084 boundaries of energetic protons. *Annales Geophysicae*, *33*(8), 1059–1070.
1085 Retrieved from <http://www.ann-geophys.net/33/1059/2015/> doi:
1086 10.5194/angeo-33-1059-2015
- 1087 Sergeev, V. A., & Gvozdevsky, B. B. (1995). MT-index – a possible new index to
1088 characterize the magnetic configuration of magnetotail. *Annales Geophysicae*,
1089 *13*(10), 1093–1103. Retrieved from [http://www.ann-geophys.net/13/1093/](http://www.ann-geophys.net/13/1093/1995/)
1090 1995/ doi: 10.1007/s00585-995-1093-9
- 1091 Sergeev, V. A., Kornilova, T. A., Kornilov, I. A., Angelopoulos, V., Kubyshk-
1092 ina, M. V., Fillingim, M., ... Larson, D. (2010, feb). Auroral signa-
1093 tures of the plasma injection and dipolarization in the inner magneto-
1094 sphere. *Journal of Geophysical Research: Space Physics*, *115*(A2), A02202.
1095 Retrieved from <http://doi.wiley.com/10.1029/2009JA014522> doi:
1096 10.1029/2009JA014522
- 1097 Sergeev, V. A., Malkov, M., & Mursula, K. (1993, may). Testing the isotropic
1098 boundary algorithm method to evaluate the magnetic field configuration in
1099 the tail. *Journal of Geophysical Research: Space Physics*, *98*(A5), 7609–
1100 7620. Retrieved from <http://doi.wiley.com/10.1029/92JA02587> doi:
1101 10.1029/92JA02587
- 1102 Singer, H., Matheson, L., Grubb, R., Newman, A., & Bouwer, D. (1996, oct). Moni-
1103 toring space weather with the GOES magnetometers. In E. R. Washwell (Ed.),
1104 *Proceedings of SPIE* (Vol. 2812, pp. 299–308). International Society for Optics
1105 and Photonics. Retrieved from [http://proceedings.spiedigitallibrary](http://proceedings.spiedigitallibrary.org/proceeding.aspx?articleid=1021197)
1106 [.org/proceeding.aspx?articleid=1021197](http://proceedings.spiedigitallibrary.org/proceeding.aspx?articleid=1021197) doi: 10.1117/12.254077
- 1107 Søråas, F. (1972). ESRO IA/B Observations at High Latitudes of Trapped and
1108 Precipitating Protons with Energies above 100 keV. In *Earth's magnetospheric*
1109 *processes* (pp. 120–132). Springer, Dordrecht. Retrieved from <http://www>

- 1110 .springerlink.com/index/10.1007/978-94-010-2896-7_12 doi: 10.1007/
1111 978-94-010-2896-7_12
- 1112 Søråas, F., Aarsnes, K., Oksavik, K., & Evans, D. S. (2002). Ring current inten-
1113 sity estimated from low-altitude proton observations. *Journal of Geophysical*
1114 *Research*, 107(A7), 1149. Retrieved from [http://doi.wiley.com/10.1029/
1115 2001JA000123](http://doi.wiley.com/10.1029/2001JA000123) doi: 10.1029/2001JA000123
- 1116 Søråas, F., Lundblad, J., Maltseva, N., Troitskaya, V., & Selivanov, V. (1980,
1117 apr). A comparison between simultaneous I.P.D.P. groundbased observa-
1118 tions and observations of energetic protons obtained by satellites. *Plan-*
1119 *etary and Space Science*, 28(4), 387–405. Retrieved from [https://
1120 www.sciencedirect.com/science/article/pii/0032063380900434](https://www.sciencedirect.com/science/article/pii/0032063380900434) doi:
1121 10.1016/0032-0633(80)90043-4
- 1122 Tapping, K. F. (2013, jul). The 10.7 cm solar radio flux (F 10.7). *Space Weather*,
1123 11(7), 394–406. Retrieved from <http://doi.wiley.com/10.1002/swe.20064>
1124 doi: 10.1002/swe.20064
- 1125 Toffoletto, F., Sazykin, S., Spiro, R., & Wolf, R. (2003). Inner magnetospheric mod-
1126 eling with the Rice Convection Model. *Space Sci. Rev.*, 107(1-2), 175–196. doi:
1127 10.1023/A:1025532008047
- 1128 Tóth, G., Sokolov, I. V., Gombosi, T. I., Chesney, D. R., Clauer, C. R., De Zeeuw,
1129 D. L., ... Kóta, J. (2005). Space Weather Modeling Framework: A new
1130 tool for the space science community. *Journal of Geophysical Research:*
1131 *Space Physics*, 110(A12). Retrieved from [http://dx.doi.org/10.1029/
1132 2005JA011126](http://dx.doi.org/10.1029/2005JA011126) doi: 10.1029/2005JA011126
- 1133 Tsyganenko, N. A. (1982, may). Pitch-angle scattering of energetic particles
1134 in the current sheet of the magnetospheric tail and stationary distribution
1135 functions. *Planetary and Space Science*, 30(5), 433–437. Retrieved from
1136 <https://www.sciencedirect.com/science/article/pii/0032063382900526>
1137 doi: 10.1016/0032-0633(82)90052-6
- 1138 Tsyganenko, N. A. (1989, jan). A magnetospheric magnetic field model with a
1139 warped tail current sheet. *Planetary and Space Science*, 37(1), 5–20. Re-
1140 trieved from [https://www.sciencedirect.com/science/article/pii/
1141 0032063389900664](https://www.sciencedirect.com/science/article/pii/0032063389900664) doi: 10.1016/0032-0633(89)90066-4
- 1142 Tsyganenko, N. A. (2002, aug). A model of the near magnetosphere with a dawn-

- 1143 dusk asymmetry 1. Mathematical structure. *Journal of Geophysical Research:*
 1144 *Space Physics*, 107(A8), SMP 12–1–SMP 12–15. Retrieved from <http://doi>
 1145 [.wiley.com/10.1029/2001JA000219](http://doi.wiley.com/10.1029/2001JA000219) doi: 10.1029/2001JA000219
- 1146 Tsyganenko, N. A., & Andreeva, V. A. (2016, nov). An empirical RBF model
 1147 of the magnetosphere parameterized by interplanetary and ground-based
 1148 drivers. *Journal of Geophysical Research: Space Physics*, 121(11), 10,786–
 1149 10,802. Retrieved from <http://doi.wiley.com/10.1002/2016JA023217> doi:
 1150 10.1002/2016JA023217
- 1151 Tsyganenko, N. A., & Sitnov, M. I. (2005, mar). Modeling the dynamics of the in-
 1152 ner magnetosphere during strong geomagnetic storms. *Journal of Geophysical*
 1153 *Research*, 110(A3), A03208. Retrieved from <http://doi.wiley.com/10.1029/>
 1154 [2004JA010798](http://doi.wiley.com/10.1029/2004JA010798) doi: 10.1029/2004JA010798
- 1155 Welling, D. T., & Liemohn, M. W. (2016, jun). The ionospheric source of magneto-
 1156 spheric plasma is not a black box input for global models. *Journal of Geophys-*
 1157 *ical Research: Space Physics*, 121(6), 5559–5565. Retrieved from <http://doi>
 1158 [.wiley.com/10.1002/2016JA022646](http://doi.wiley.com/10.1002/2016JA022646) doi: 10.1002/2016JA022646
- 1159 West, H. I., Buck, R. M., & Kivelson, M. G. (1978, aug). On the configuration
 1160 of the magnetotail near midnight during quiet and weakly disturbed periods:
 1161 Magnetic field modeling. *Journal of Geophysical Research*, 83(A8), 3819.
 1162 Retrieved from <http://doi.wiley.com/10.1029/JA083iA08p03819> doi:
 1163 10.1029/JA083iA08p03819
- 1164 Wolf, R. A., Harel, M., Spiro, R. W., Voigt, G.-H., Reiff, P. H., & Chen, C. K.
 1165 (1982). Computer simulation of inner magnetospheric dynamics for the
 1166 magnetic storm of July 29, 1977. *Journal of Geophysical Research*, 87(A8),
 1167 5949–5962. doi: 10.1029/JA087iA08p05949
- 1168 Yahnin, A. G., & Yahnina, T. A. (2007, oct). Energetic proton precipitation related
 1169 to ion-cyclotron waves. *Journal of Atmospheric and Solar-Terrestrial Physics*,
 1170 69(14), 1690–1706. Retrieved from [https://www.sciencedirect.com/](https://www.sciencedirect.com/science/article/pii/S1364682607001885)
 1171 [science/article/pii/S1364682607001885](https://www.sciencedirect.com/science/article/pii/S1364682607001885) doi: 10.1016/j.jastp.2007.02.010
- 1172 Yue, C., Wang, C.-P., Lyons, L., Liang, J., Donovan, E. F., Zaharia, S. G., & Hen-
 1173 derson, M. (2014, oct). Current sheet scattering and ion isotropic boundary
 1174 under 3-D empirical force-balanced magnetic field. *Journal of Geophysi-*
 1175 *cal Research: Space Physics*, 119(10), 8202–8211. Retrieved from <http://>

1176 doi.wiley.com/10.1002/2014JA020172 doi: 10.1002/2014JA020172
1177 Zhang, Y., Paxton, L. J., & Zheng, Y. (2008, jan). Interplanetary shock induced ring
1178 current auroras. *Journal of Geophysical Research: Space Physics*, 113(A1),
1179 A01212. Retrieved from <http://doi.wiley.com/10.1029/2007JA012554> doi:
1180 10.1029/2007JA012554

Author Manuscript

Figure 1.

Author Manuscript

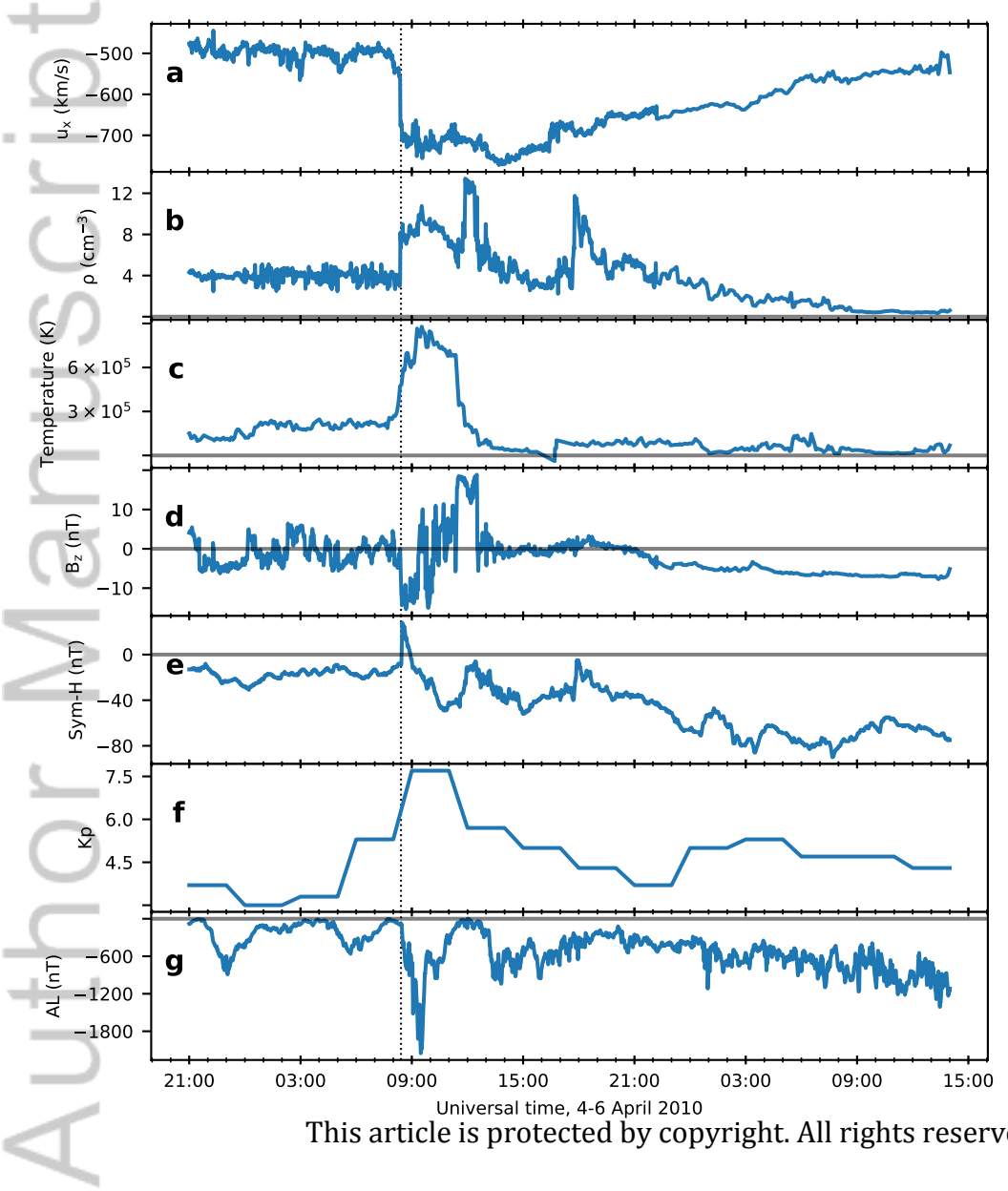


Figure 2.

Author Manuscript

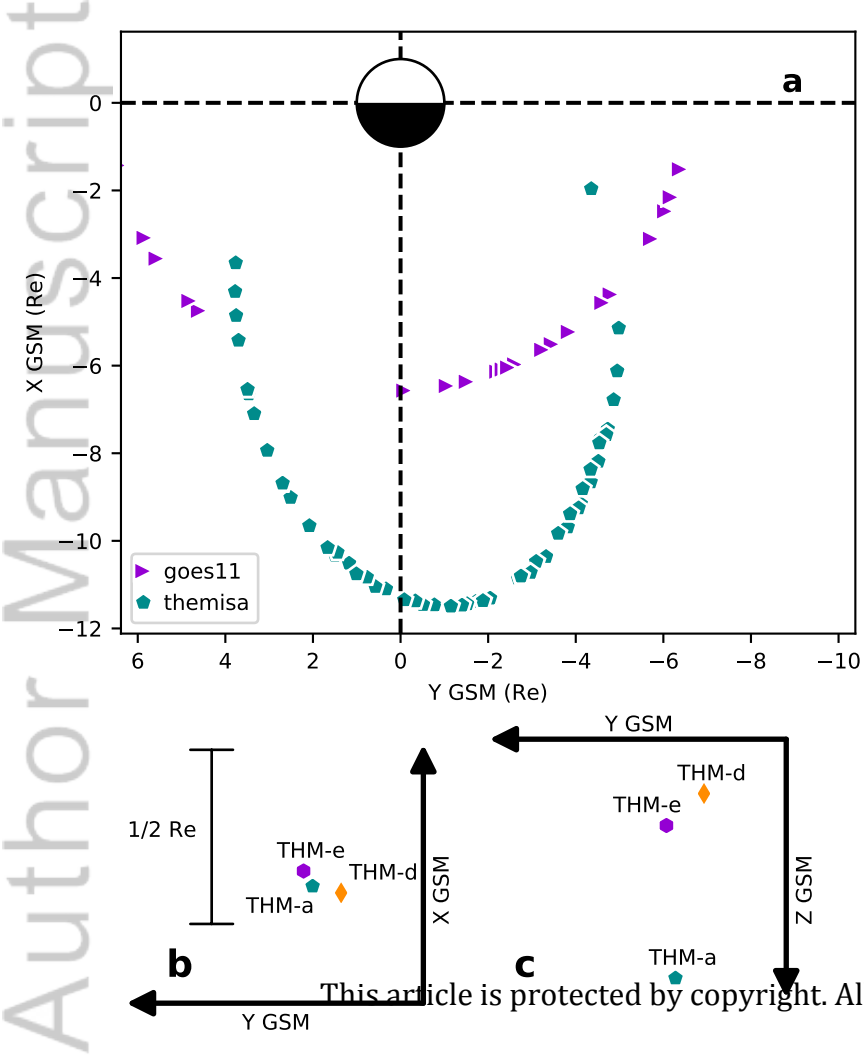
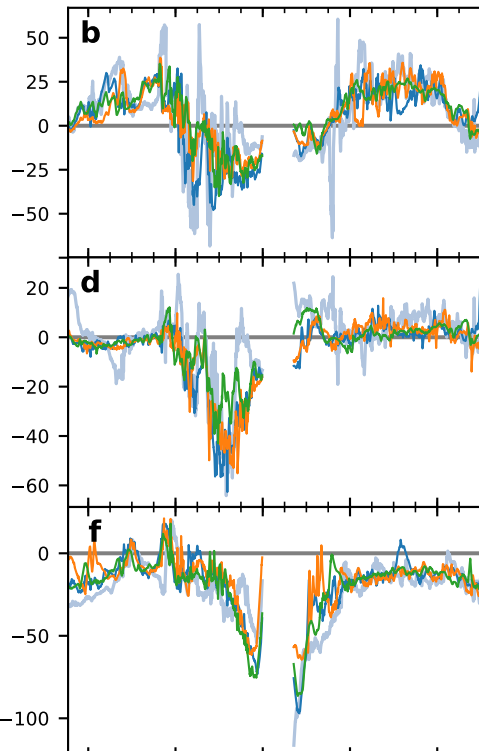
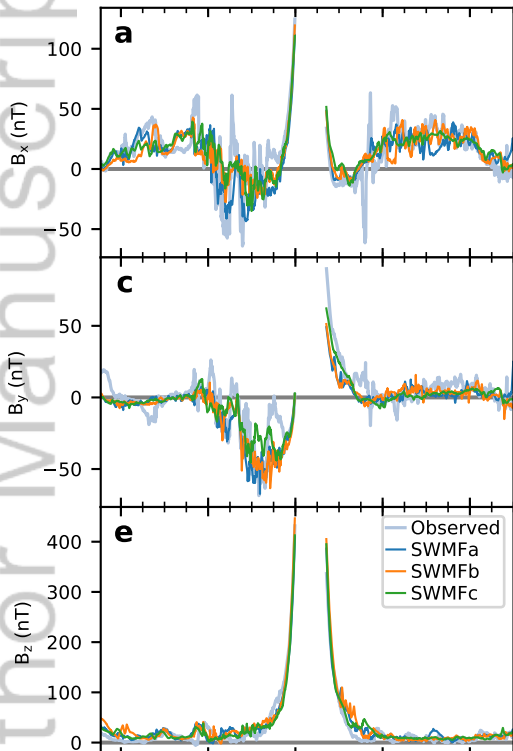


Figure 3.

Author Manuscript

Total Field

External Field



UT	02:00	10:00	18:00	02:00	10:00	02:00	10:00	18:00	02:00	10:00
MLT	23.2	1.02	5.17	23.2	0.979	23.2	1.02	5.17	23.2	0.979
X GSM	-9.66	-10.7	-0.841	-9.68	-10.7	-9.66	-10.7	-0.841	-9.68	-10.7
Y GSM	1.97	-2.95	-3.11	1.97	-2.95	1.97	-2.95	-3.11	1.97	-2.95
Z GSM	0.213	1.19	0.301	0.295	1.25	0.213	1.19	0.301	0.295	1.25

Figure 4.

Author Manuscript

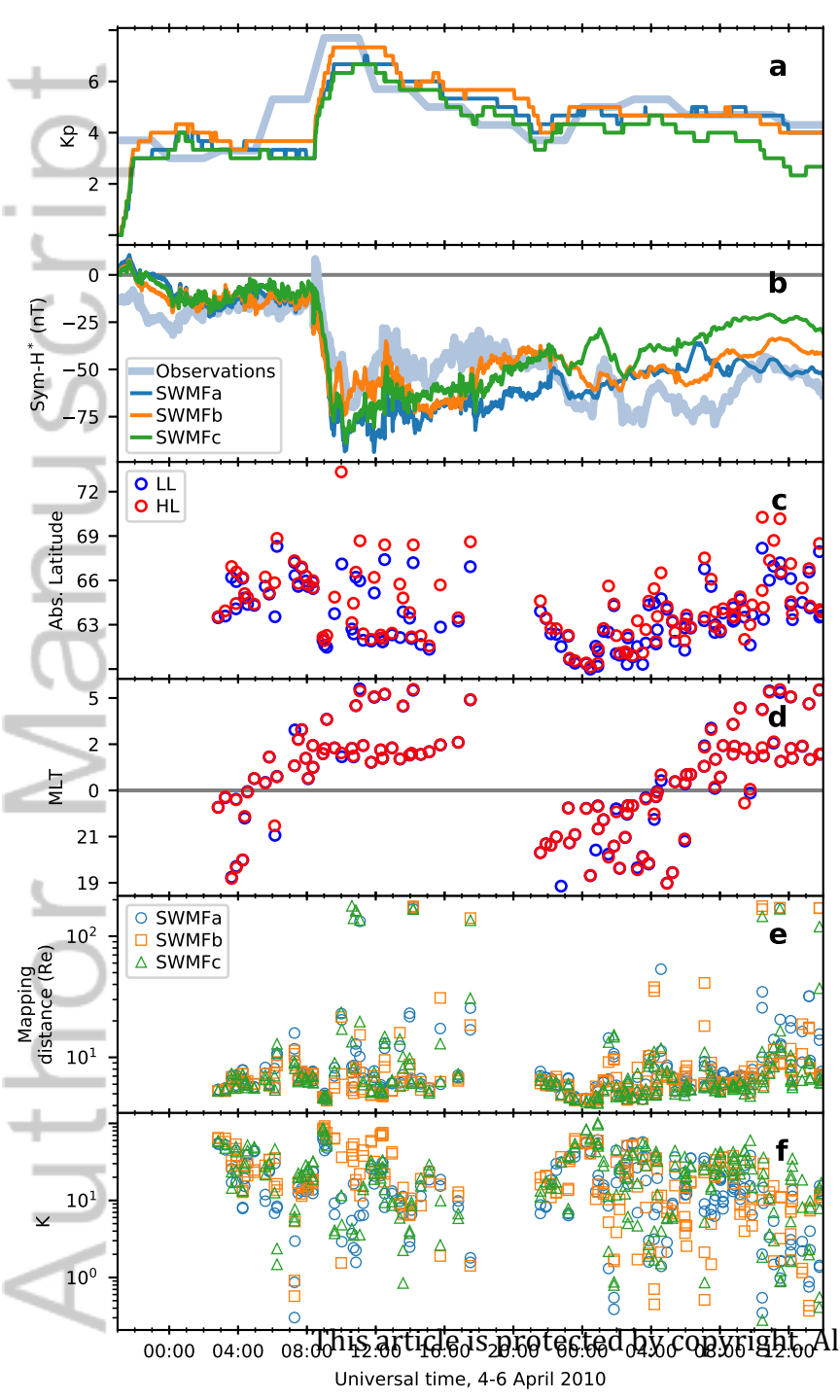


Figure 5.

Author Manuscript

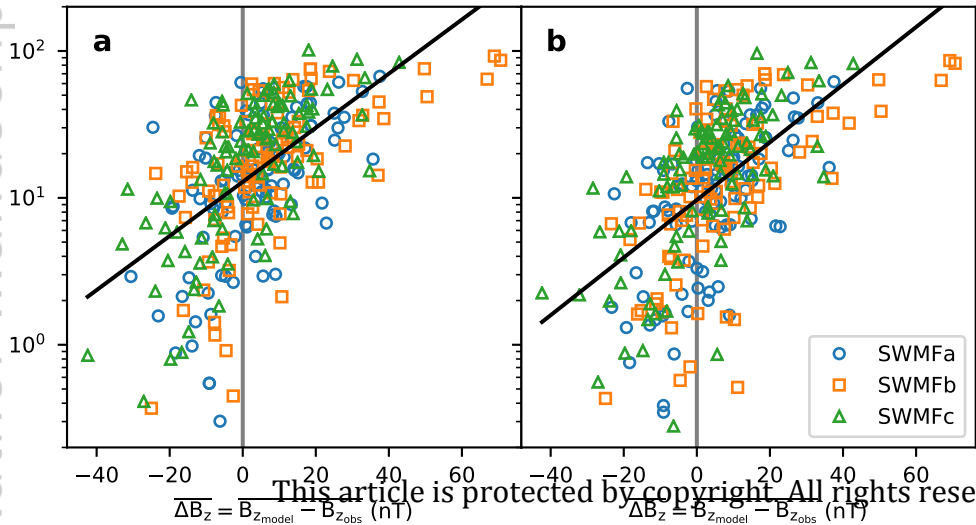


Figure 6.

Author Manuscript

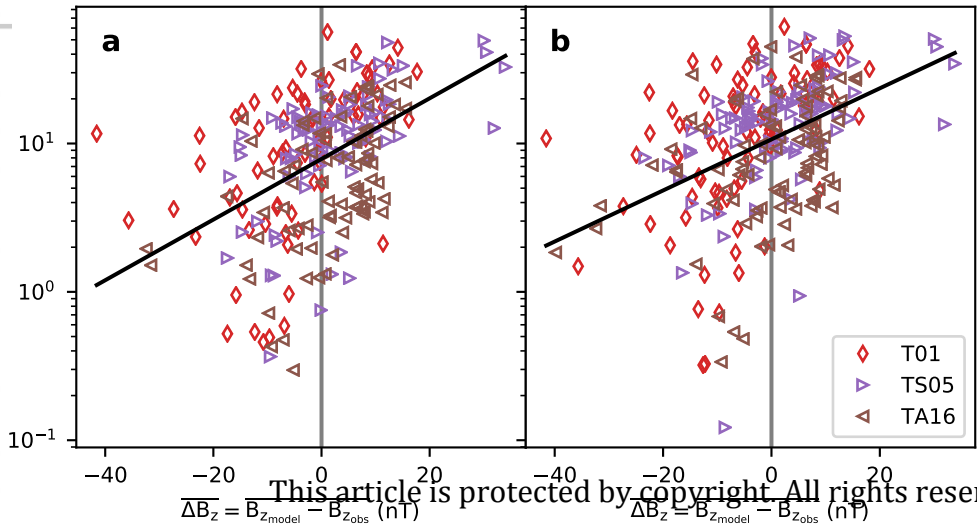


Figure 7.

Author Manuscript

SWMF

Empirical

SWMF+Empirical

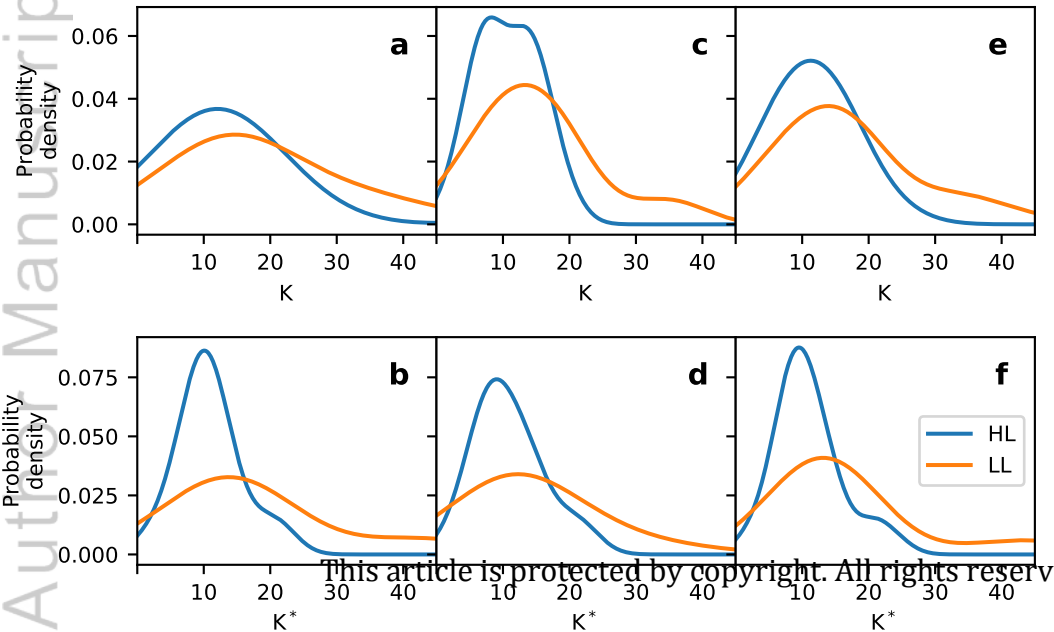
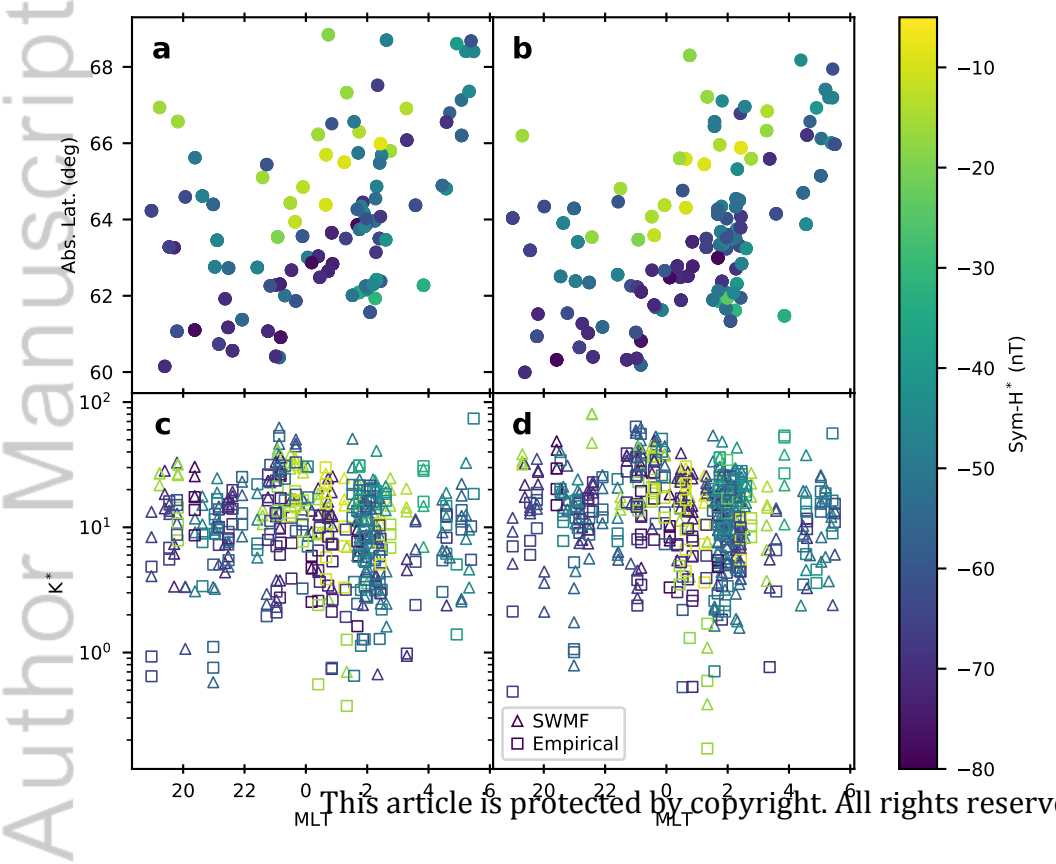
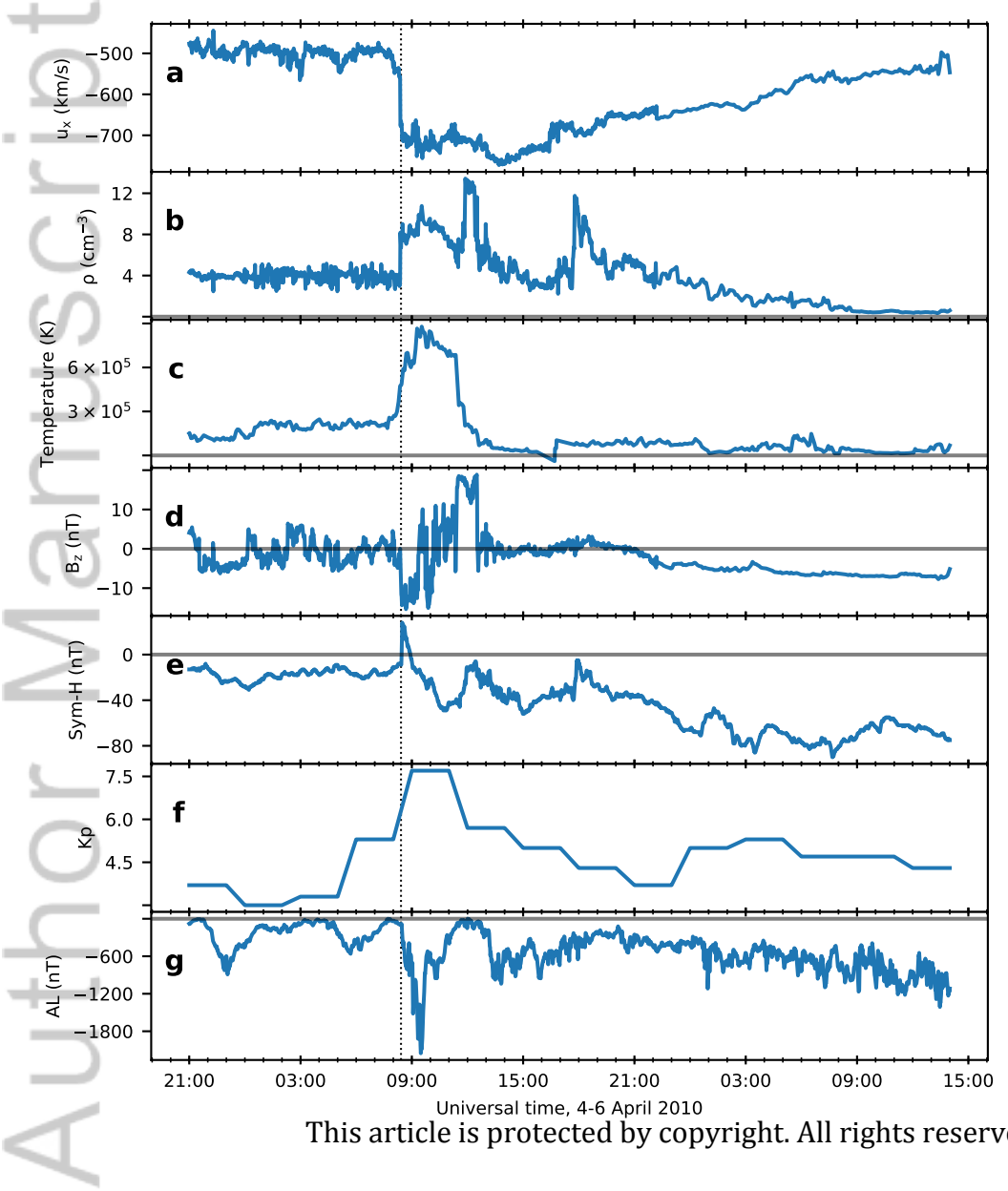
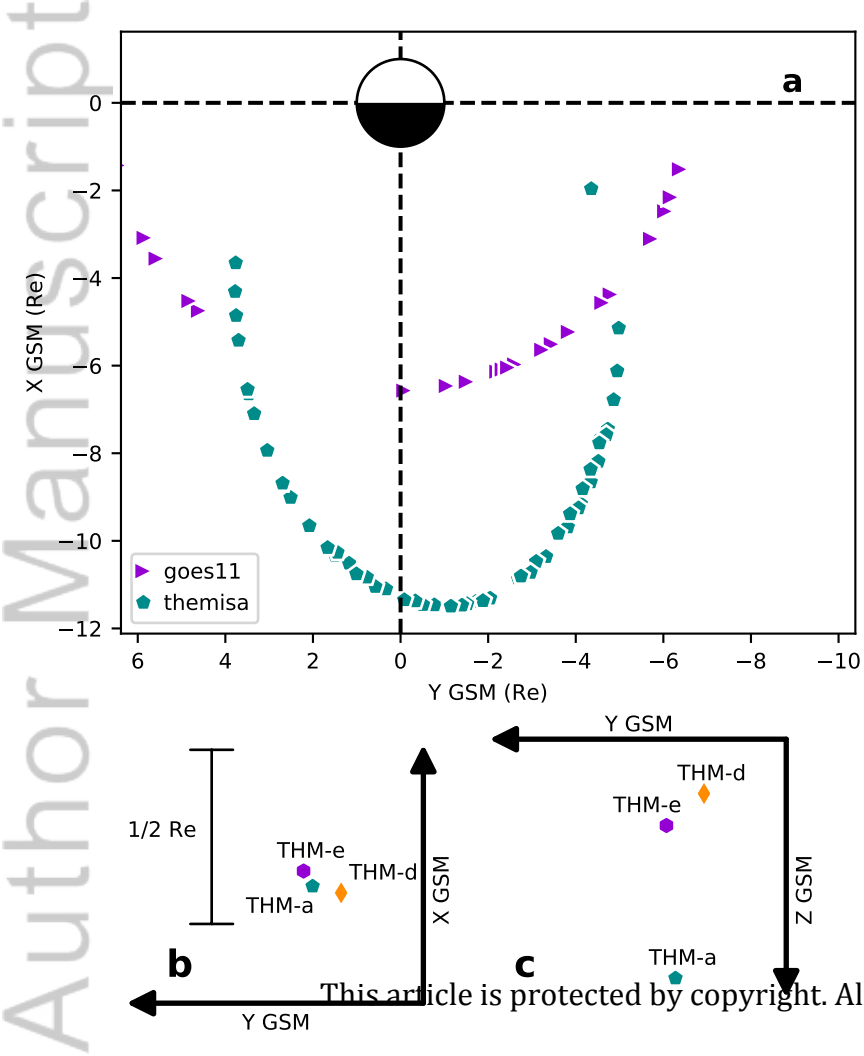


Figure 8.

Author Manuscript

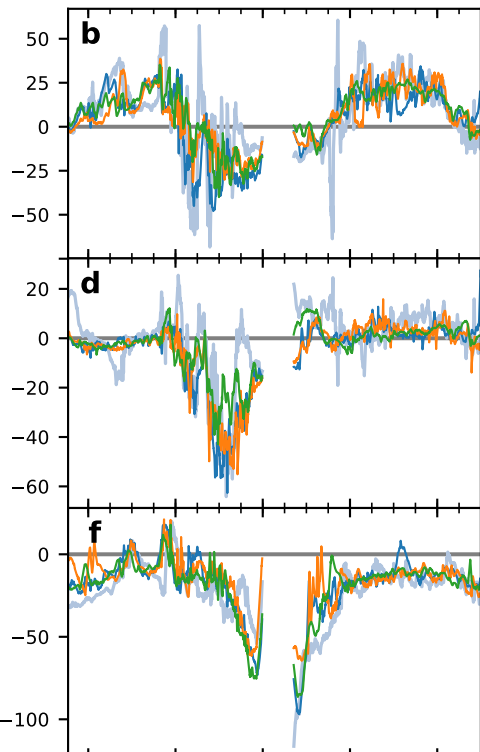
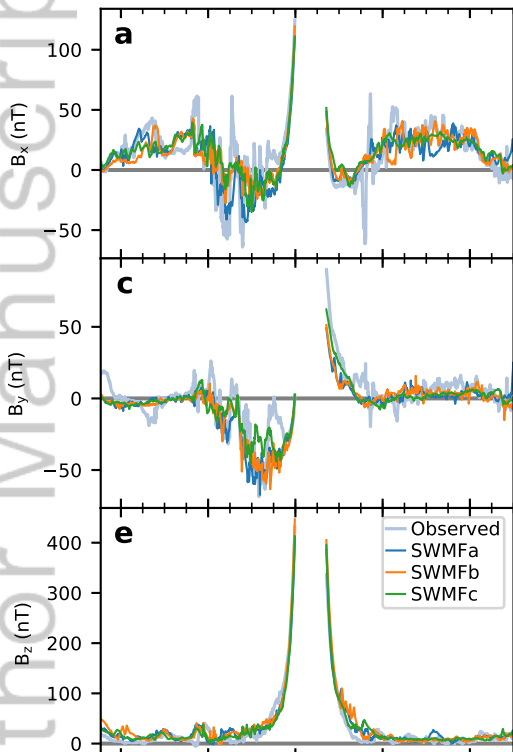




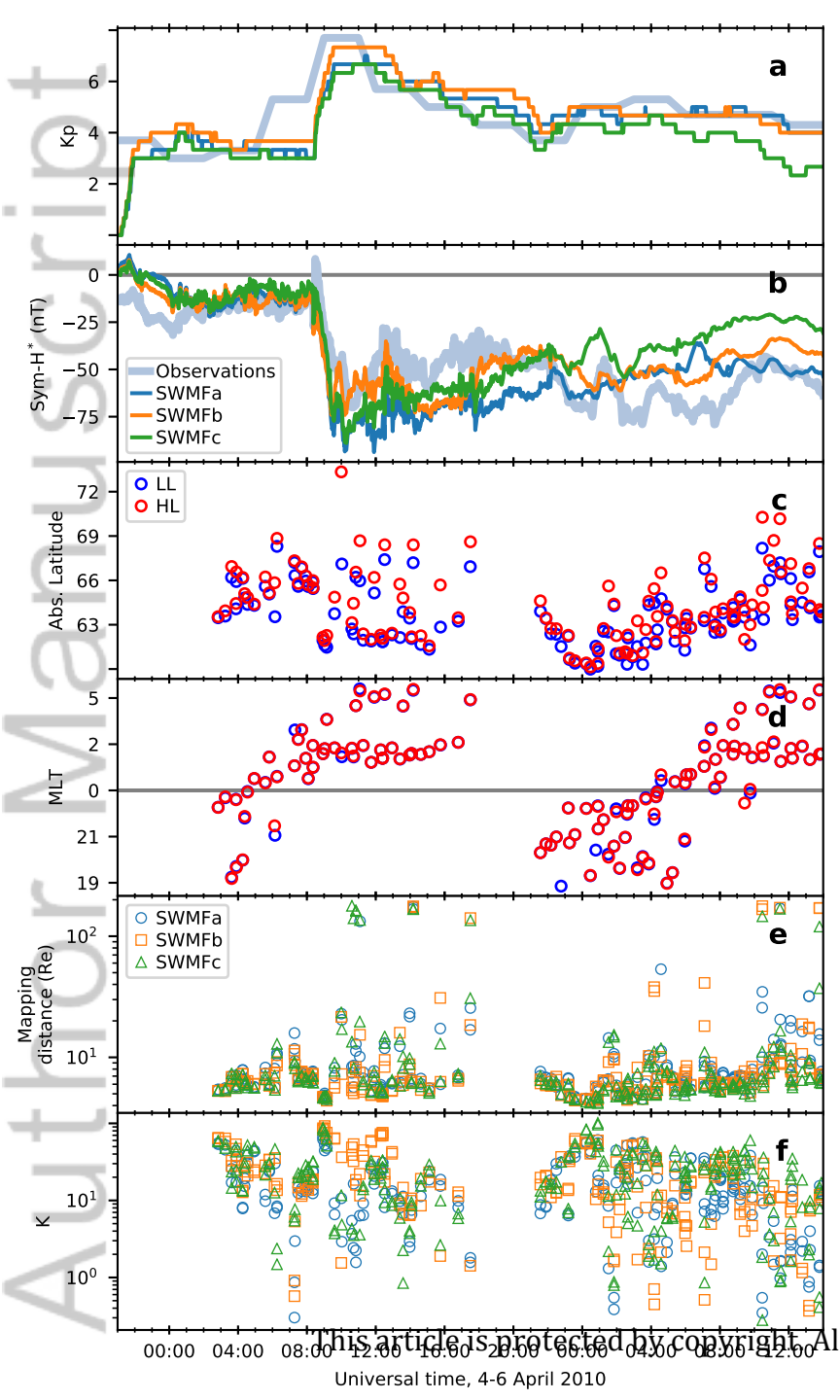


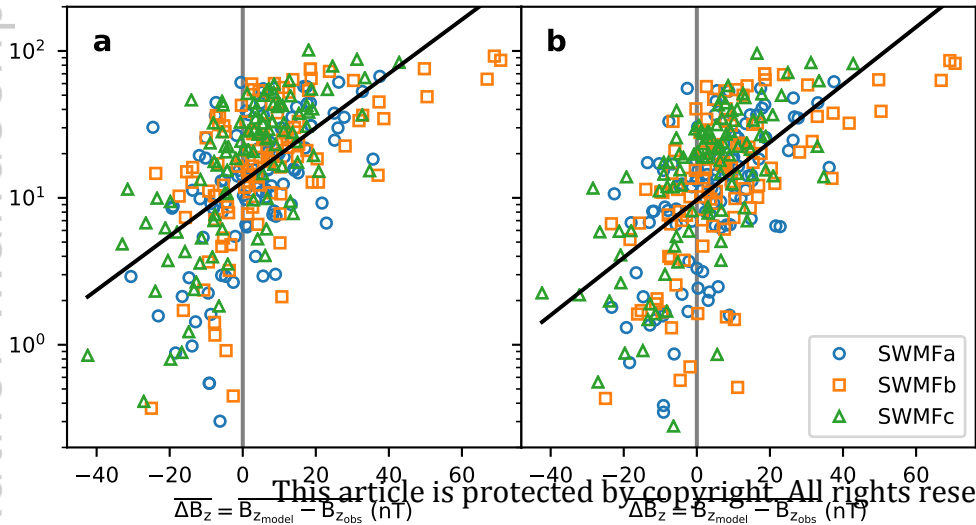
Total Field

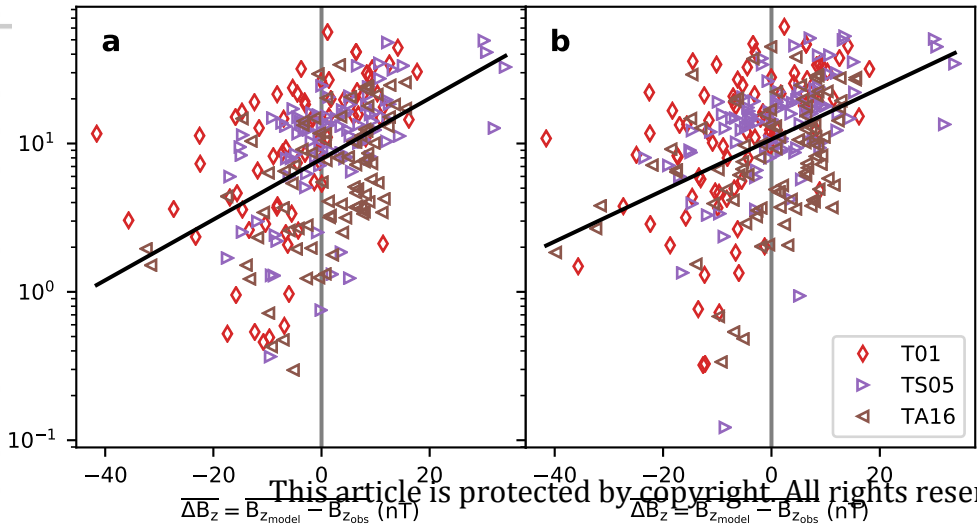
External Field



UT	02:00	10:00	18:00	02:00	10:00	02:00	10:00	18:00	02:00	10:00
MLT	23.2	1.02	5.17	23.2	0.979	23.2	1.02	5.17	23.2	0.979
X GSM	-9.66	-10.7	-0.841	-9.68	-10.7	-9.66	-10.7	-0.841	-9.68	-10.7
Y GSM	1.97	-2.95	-3.11	1.97	-2.95	1.97	-2.95	-3.11	1.97	-2.95
Z GSM	0.213	1.19	0.301	0.295	1.25	0.213	1.19	0.301	0.295	1.25







SWMF

Empirical

SWMF+Empirical

